

HST / ACS EMISSION LINE IMAGING OF LOW REDSHIFT 3CR RADIO GALAXIES I: THE DATA¹

GRANT R. TREMBLAY^{2,4}, MARCO CHIABERGE^{2,3}, WILLIAM B. SPARKS², STEFI A. BAUM⁴, MARK G. ALLEN⁵, DAVID J. AXON⁴,
ALESSANDRO CAPETTI⁶, DAVID J. E. FLOYD⁷, F. DUCCIO MACCHETTO², GEORGE K. MILEY⁷, JACOB NOEL-STORR⁴,
CHRISTOPHER P. O'DEA⁴, ERIC S. PERLMAN⁹, AND ALICE C. QUILLEN¹⁰

Accepted for publication in *ApJS*

ABSTRACT

We present 19 nearby ($z < 0.3$) 3CR radio galaxies imaged at low- and high-excitation as part of a Cycle 15 *Hubble Space Telescope* snapshot survey with the Advanced Camera for Surveys. These images consist of exposures of the H α (6563 Å, plus [NII] contamination) and [OIII] λ 5007 emission lines using narrow-band linear ramp filters adjusted according to the redshift of the target. To facilitate continuum subtraction, a single-pointing 60 s line-free exposure was taken with a medium-band filter appropriate for the target's redshift. We discuss the steps taken to reduce these images independently of the automated recalibration pipeline so as to use more recent ACS flat-field data as well as to better reject cosmic rays. We describe the method used to produce continuum-free (pure line-emission) images, and present these images along with qualitative descriptions of the narrow-line region morphologies we observe. We present H α + [NII] and [OIII] line fluxes from aperture photometry, finding the values to fall expectedly on the redshift-luminosity trend from a past *HST*/WFPC2 emission line study of a larger, generally higher redshift subset of the 3CR. We also find expected trends between emission line luminosity and total radio power, as well as a positive correlation between the size of the emission line region and redshift. We discuss the associated interpretation of these results, and conclude with a summary of future work enabled by this dataset.

Subject headings: galaxies: active — galaxies: emission lines — radio continuum: galaxies

1. INTRODUCTION

Characteristically intense nuclear emission in radio galaxies, along with the highly collimated jets powered by accretion onto their central engines, can influence star formation, excitation and ionization of the ISM, as well as provide kinetic stresses on the hot X-ray emitting coronal gas that pervades clusters of galaxies (Quillen & Bower 1999; McNamara et al. 2000; Blanton et al. 2001; Reynolds et al. 2002; Ruszkowski & Begelman 2002). Narrow-band imaging surveys of radio galaxies at redshifts $z > 0.6$ were among the first studies to establish such a connection, having shown the optical line-emitting gas ($T \sim 10^4$ K) near the nuclei of these objects to spatially align with the radio jet axes on kiloparsec scales (Fosbury 1986; Hansen et al. 1987; Baum et al. 1988; McCarthy 1988; Baum et al. 1990). This so-called ‘alignment effect’ has been attributed to shocks induced by

propagation of the radio jet, as well as photoionization from the AGN (e.g., Baum & Heckman 1989a; McCarthy 1993; Best et al. 2000). While these shocks can trigger star formation along the regions of the ISM excited into line emission (Chambers et al. 1987), more recent work has suggested that feedback from the AGN may also play a role in ultimately quenching the star formation rate (SFR) in the late stages of the host galaxy's evolution, thereby ushering its rapid passage from the ‘blue cloud’ to the ‘red sequence’ (e.g., Cowie et al. 1996; Bell et al. 2004; Faber et al. 2007, and references therein). Work is ongoing in reconciling the seemingly competing roles of AGN feedback in both inducing, then possibly truncating star formation at successive stages of galactic evolution (e.g., Silk & Rees 1998; Fabian 1999; di Matteo et al. 2005; Hopkins et al. 2005; Silverman et al. 2008). Regardless, it is clear that the AGN and its host galaxy share dependent evolutionary paths (e.g., Magorrian et al. 1998; Ferrarese & Merritt 2000; Gebhardt et al. 2000), and that studies of the ionized nuclear gas in radio galaxies, as unique probes of the early universe, will be key to understanding this relationship on size and time scales small and large.

The *Hubble Space Telescope* (*HST*) has undertaken systematic surveys of the 3CR catalog of radio galaxies in the UV (Allen et al. 2002), optical (Martel et al. 1999; de Koff et al. 2000; Privon et al. 2008), and near-infrared (Madrid et al. 2006; Donzelli et al. 2007; Tremblay et al. 2007; Floyd et al. 2008). These programs, in concert with a robust array of ground-based observations of the 3CR in nearly all wavelength regimes, have established a uniform database of cross-spectrum imaging and spectroscopy for a sample that is nearly complete with redshift and flux limit, unbiased with respect to optical/IR wavelengths, and containing galaxies exhibiting a variety of intrinsic characteristics. The completeness and diversity of the sample has enabled studies into radio-loud unification models and the dichotomy between relatively low power, edge-darkened Fanaroff and Riley class I radio galax-

¹ Based on observations made with the NASA/ESA *Hubble Space Telescope*, obtained at the Space Telescope Science Institute, which is operated by the Association of Universities for Research in Astronomy, Inc., under NASA contract 5-26555

² Space Telescope Science Institute, 3700 San Martin Drive, Baltimore, MD 21218; grant@stsci.edu

³ INAF—Istituto di Radioastronomia, Via P. Gobetti 101, Bologna I-40129, Italy

⁴ Rochester Institute of Technology, 84 Lomb Memorial Drive, Rochester, NY 14623; grant@astro.rit.edu

⁵ Centre de Données Astronomique, 11 Rue de l'Université, 67000 Strasbourg, France

⁶ INAF—Osservatorio Astronomico di Torino, Strada Osservatorio 20, 10025 Pino Torinese, Italy

⁷ Las Campanas Observatory, Observatories of the Carnegie Institute of Washington, Casilla 601, La Serena, Chile

⁸ Leiden Observatory, P.O. Box 9513, NL-2300 RA Leiden, The Netherlands

⁹ Physics and Space Sciences Department, Florida Institute of Technology, 150 West University Boulevard, Melbourne, FL 32901

¹⁰ Department of Physics and Astronomy, University of Rochester, 600 Wilson Boulevard, Rochester, NY 14627

ies (hereafter FR I, Fanaroff & Riley 1974) and higher power, edge-brightened FR II radio galaxies (Chiaberge et al. 2000, 2002). *HST* observations of the 3CR have also led to discoveries of new optical and IR jets (Floyd et al. 2006), a trend between nuclear dusty disk inclination and host galaxy isophotal shapes (Tremblay et al. 2007) and face on disks with optical jets (Sparks et al. 2000). Jet/disk orientations were studied at unprecedented spatial resolution (e.g., Schmitt et al. 2002; Verdoes Kleijn & de Zeeuw 2005; Tremblay et al. 2006, and references therein). Allen et al. (2002) also found complex UV morphologies unlike those seen in quiescent hosts, indicative of ongoing star formation.

In this paper we present narrow-band emission line observations of 19 nearby ($z < 0.3$) 3CR radio galaxies imaged at low- and high- excitation with the Advanced Camera for Surveys (ACS) aboard *HST*. These images of the warm optical line ($H\alpha$ and $[OIII]\lambda 5007$) emitting gas present in the nuclei of the radio galaxies in our sample offer the highest sensitivity and spatial resolution yet available in the *HST* 3CR database. This enables detailed studies of shocked and star-forming regions of the ISM in relation to radio jets, providing the already rich 3CR dataset with a larger framework from which to study the various phenomena discussed above.

We organize this paper as follows. In §2 we describe these *HST* observations in detail, and in §3 we discuss the associated data reduction. In §4 we present the $H\alpha + [NII]$ (low-excitation) and $[OIII]$ (high-excitation) emission line images, as well as qualitative descriptions of each. We also provide emission line luminosity results and an associated discussion. We summarize this work and discuss future studies enabled by this new dataset in §5. Throughout this paper we use $H_0 = 71$ km s⁻¹ Mpc⁻¹, $\Omega_M = 0.27$, and $\Omega_\Lambda = 0.73$.

2. SAMPLE SELECTION & OBSERVATIONS

In this paper we present 19 radio galaxies from the low-redshift ($z < 0.3$) extragalactic subset of the Revised Third Cambridge Catalog (3CR, Bennett 1962b,a; Spinrad et al. 1985). 3CR sources are selected by radio flux density at 178 MHz, at which extended, unbeamed lobes are detected irrespective of the radio jet's orientation with respect to the line of sight. The sample is therefore free from orientation bias and is nearly complete with redshift, providing a strong framework for statistical analysis important for studies of (e.g.) radio-loud unification models. Moreover, the sample consists of radio galaxies that exhibit a wide variety of characteristics (size, shape, jet morphology, radio luminosity, FR type, dust content, etc.), allowing for physical comparisons to be made among properties intrinsic to various species of radio-loud AGN. We select the low-redshift subset of the 3CR so as to achieve the highest possible spatial resolution, in addition to requiring the $H\alpha$ line to be within the redshift range of high sensitivity to provide uniform line ratio mapping.

Of the 116 extragalactic 3CR sources with $z < 0.3$, 98 were awarded for observation in the Cycle 15 ACS snapshot program 10882 (PI: Sparks). The remaining 18 targets that were not requested in our proposal were excluded for various reasons, mainly due to emission line data already being present in the archive for that object. Ultimately, 20 of our awarded targets were observed prior to failure of ACS side two electronics in January 2007. Of these observations, 19 were successful. Our observation of 3C 371 was carried out but unsuccessful due to failure of guide star acquisition, resulting in unusable data. The sample consists of 4 FR I radio galaxies, 12 FR II radio galaxies, and 3 targets exhibiting compact

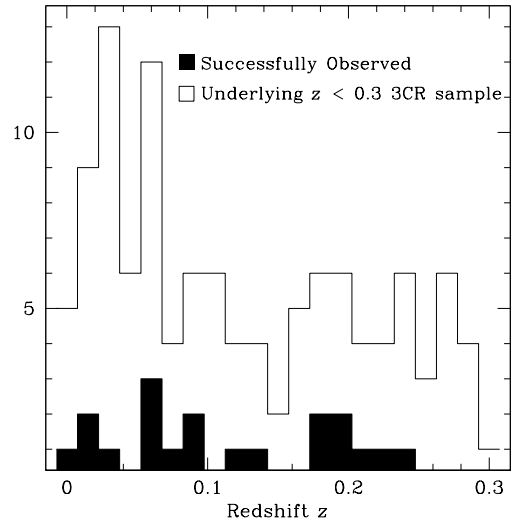


FIG. 1.— Redshift distribution of the low redshift ($z < 0.3$) extragalactic subset of the 3CR sample (116 galaxies), compared with the distribution of targets successfully imaged (prior to ACS failure) as part of the ACS snapshot program presented in this paper (solid, 19 galaxies). While this dataset represents a small fraction of the underlying sample, it spans nearly the entire range of redshift. Collectively, the vast majority of the underlying sample has been imaged as part of past *HST* programs in the UV, optical, and near IR. See §1 for a summary of these *HST* programs.

steep spectrum (CSS) or undiscernible radio morphology.

While only a small subset of our initially proposed sample was observed, the nature of *HST*'s snapshot mode means that observations were scheduled by convenience with respect to *HST*'s other programs at the time, and not by any selection effect. Our group of galaxies is therefore as unbiased as the 3CR itself. Moreover, the 19 galaxies successfully observed span nearly the whole redshift range ($0.0075 < z < 0.224$, see Fig. 1) of the underlying sample and, as we will discuss in more detail in §4, includes galaxies exhibiting a wide array of emission line characteristics.

Our 19 successful observations consist of ACS Wide Field Channel (WFC) exposures of the $H\alpha + [NII]$ and $[OIII]\lambda 5007$ emission lines using narrow-band (2% bandpass) linear ramp filters (LRFs) at wavelengths adjusted according to the redshift of the target (see Table 1). The LRFs aboard ACS feature effective central bandwidths that vary as the filter is rotated across the FOV. While the LRFs are useful in providing the observer narrow-band imaging capabilities at a wide variety of central wavelengths, there is a drawback in that the target is imaged monochromatically only over a small region ($\sim 40'' \times 80''$) of the instrument's FOV. In planning the observations for this dataset, we ensured that the target galaxy nuclei always corresponded to the very center of this region.

With each target fully observed in one orbit, an exposure time of 2×200 s and 2×250 s was used for the $H\alpha$ and $[OIII]$ lines, respectively, with a two point dither pattern (of line spacing $0''.145$) to aide cosmic ray and hot pixel rejection. So as to facilitate continuum subtraction from the emission line images, a 60 s, single pointing exposure was taken with a medium (9%) bandpass ramp filter centered at rest-frame 5500 Å, covering a region of the optical spectrum absent of significant contamination from line emission. Subarrays were used to increase the efficiency of these observations, allowing 4 images to be stored in the ACS buffer at once. The WFC on ACS consists of two 2048×4096 pixel CCDs (WFC1 and WFC2), each with a plate scale of $0''.049$ per pixel and a field

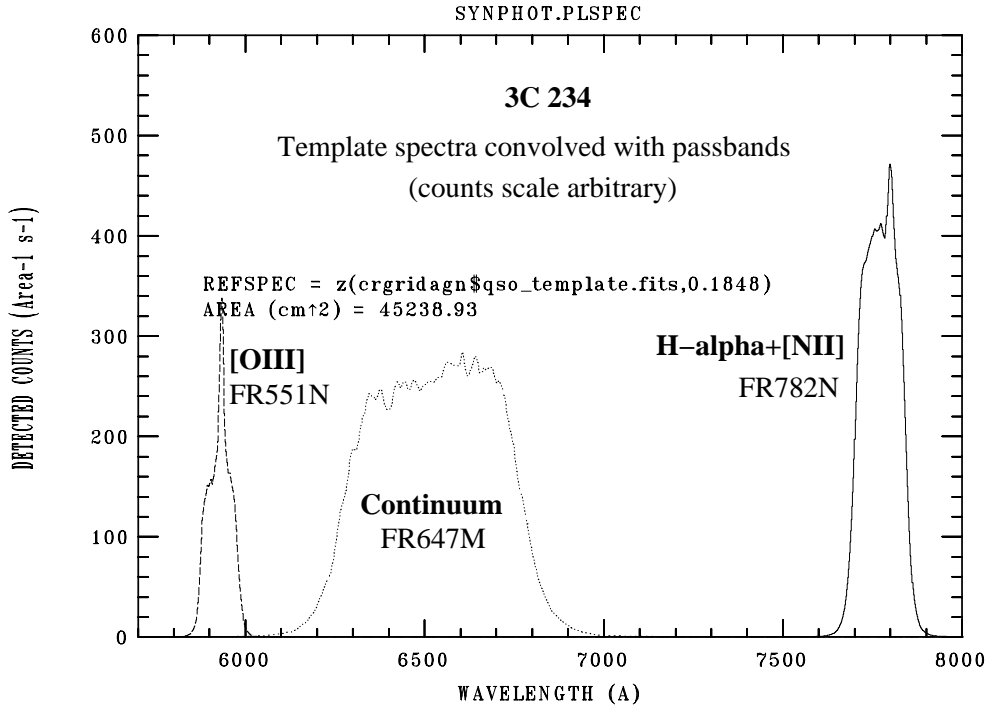


FIG. 2.— A representative example of our filter selection strategy. We have convolved *template* LINER (chosen only for example $H\alpha$ and $[NII]$ lines) and QSO (for $[OIII]$) spectra through the filters chosen for our observations of 3C 234 ($z = 0.18$) as an example. The spectra are used only as an illustration, and are not meant for quantitative discussion. The counts scale is therefore arbitrary. See §2 for details on our filter selection strategy.

of view (FOV) of $202'' \times 202''$ (further details may be found in the ACS Instrument Handbook¹¹). See Table 1 for an observation log related to this program.

It is important to note that, for all “ $H\alpha$ imaging” presented in this paper, the bandpass used was contaminated by $[NII]$ emission at 6548 and 6583 Å. References to $H\alpha$ will therefore read “ $H\alpha+[NII]$ ” throughout this paper. Though it is beyond the scope of this work to subtract this contamination, $[NII]$ flux does not impact the results presented in this paper in any way as we present all correlations with respect to $H\alpha+[NII]$ and never $H\alpha$ alone. In follow-up papers providing analysis of these data, however, new ground-based optical spectroscopy of the 3CR by Buttiglione et al. (2009) may be used to better quantify the contribution of $[NII]$ through each $H\alpha$ bandpass. The Buttiglione spectra, obtained using the Telescopio Nazionale Galileo (TNG), may be convolved with the spectral response of the *HST* ACS ramp filters, providing a constraint on the relative strength of $H\alpha$ and $[NII]$ in the filter throughput. In doing this, one must take into account the fact that the TNG spectra are extracted from a $2'' \times 2''$ region, while many of our galaxies (e.g., 3C 33) are far more extended. In Fig. 3 we plot the de-reddened flux ratios from Buttiglione et al. (2009) of the diagnostic line $[NII]\lambda 6584$ to $H\alpha$, vs. redshift, for each galaxy in our sample (with the exception of 3C 132). The results from Buttiglione et al. (2009), some of which are apparent in Fig. 3, show that the relative contributions of $[NII]$ and $H\alpha$ vary widely from source-to-source, and that $[NII]$ appears to dominate in most high-excitation galaxies (HEG, see Table 2).

3. DATA REDUCTION

Here we describe the steps taken to produce data that has been calibrated, cleaned of cosmic rays (CRs) and hot pixels, and finally subtracted of contamination from continuum emission. The *HST* On-the-Fly Recalibration (OTFR) pipeline utilizes pre-launch (ground) flats in the reduction of ACS LRF images, the use of which can contribute upwards of 7% uncertainty to reduced data given the evolution of the instrument in the years since launch. By reducing each image “manually”, we are able to avoid introducing this uncertainty, as well as implement a more proactive approach to cleaning the images of CRs and hot pixels, particularly in the case of the single-pointing continuum images for which automated CR rejection via combination of dithered images is not possible. For these reasons the images presented in this paper have been reduced independently of the OTFR pipeline, in a process we describe below.

3.1. Calibration

The calibration stage begins with the raw exposures and corrects for flat-fielding, bias and dark levels, as well as absolute sensitivity. Each of these corrections is performed by the IRAF¹² routine *calacs* (in *stdas.hst_calib.acs*). So as to avoid the uncertainty that would otherwise have been introduced by the use of pre-launch flats in the OTFR pipeline, we updated the *PFLTFILE* header keyword for each raw image to specify that the newest available flat be utilized for each *calacs* run.

¹¹ Boffi, F.R., et al. 2007, “ACS Instrument Handbook”, Version 8.0. (Baltimore: STScI).

¹² IRAF is distributed by the National Optical Astronomy Observatory, which is operated by the Association of Universities for Research in Astronomy (AURA) under cooperative agreement with the National Science Foundation.

TABLE 1
OBSERVATION LOG

Source (1)	z (2)	Obs. Date (UT) (3)	α (J2000.0) (4)	δ (J2000.0) (5)	Filters (6)	Line/Cont. (7)	λ (\AA) (8)	Exp. Time (s) (9)
3C 33.0	0.0597	20 Aug 2006	01 08 52.8	+13 20 14	FR647M	Cont.	5824	1 \times 60
					FR716N	H α	6950	2 \times 200
3C 40.0	0.0180	17 Sep 2006	01 20 34.0	-01 20 34	FR551N	[OIII]	5302	2 \times 250
					FR647M	Cont.	5593	1 \times 60
					FR656N	H α	6674	2 \times 200
3C 78.0	0.0286	13 Sep 2006	03 08 26.2	+04 06 39	FR505N	[OIII]	5092	2 \times 250
					FR647M	Cont.	5654	1 \times 60
					FR656N	H α	6747	2 \times 200
3C 93.1	0.2430	8 Sep 2006	03 48 46.9	+33 53 15	FR505N	[OIII]	5147	2 \times 250
					FR647M	Cont.	6842	1 \times 60
					FR853N	H α	8146	2 \times 200
3C 129.0	0.0208	25 Oct 2006	04 49 09.1	+45 00 39	FR601N	[OIII]	6228	2 \times 250
					FR647M	Cont.	5615	1 \times 60
					FR656N	H α	6701	2 \times 200
3C 132.0	0.2140	20 Aug 2006	04 56 43.0	+22 49 22	FR505N	[OIII]	5112	2 \times 250
					FR647M	Cont.	6677	1 \times 60
					FR782N	H α	7967	2 \times 200
3C 136.1	0.0640	4 Nov 2006	05 16 03.1	+24 58 25	FR601N	[OIII]	6078	2 \times 250
					FR647M	Cont.	5852	1 \times 60
					FR716N	H α	6983	2 \times 200
3C 180.0	0.2200	11 Nov 2006	07 27 04.5	-02 04 42	FR551N	[OIII]	5327	2 \times 250
					FR647M	Cont.	6710	1 \times 60
					FR782N	H α	8006	2 \times 200
3C 196.1	0.1980	3 Dec 2006	08 15 27.8	-03 08 27	FR601N	[OIII]	6108	2 \times 250
					FR647M	Cont.	6588	1 \times 60
					FR782N	H α	7862	2 \times 200
3C 197.1	0.1280	16 Sep 2006	08 21 33.6	+47 02 37	FR601N	[OIII]	5998	2 \times 250
					FR647M	Cont.	6215	1 \times 60
					FR716N	H α	7416	2 \times 200
3C 219.0	0.1744	5 Dec 2006	09 21 08.6	+45 38 57	FR551N	[OIII]	5657	2 \times 250
					FR647M	Cont.	6457	1 \times 60
					FR782N	H α	7704	2 \times 200
3C 227.0	0.0858	22 Jan 2007	09 47 45.1	+07 25 21	FR601N	[OIII]	5878	2 \times 250
					FR647M	Cont.	5973	1 \times 60
					FR716N	H α	7127	2 \times 200
3C 234.0	0.1848	15 Dec 2006	10 01 49.5	+28 47 09	FR551N	[OIII]	5437	2 \times 250
					FR647M	Cont.	6512	1 \times 60
					FR782N	H α	7770	2 \times 200
3C 270.0	0.0075	25 Dec 2006	12 19 23.2	+05 49 31	FR601N	[OIII]	5928	2 \times 250
					FR647M	Cont.	5541	1 \times 60
					FR656N	H α	6612	2 \times 200
3C 285.0	0.0794	11 Jan 2007	13 21 17.8	+42 35 15	FR505N	[OIII]	5044	2 \times 250
					FR647M	Cont.	5934	1 \times 60
					FR716N	H α	7081	2 \times 200
3C 314.1	0.1197	30 Dec 2006	15 10 22.5	+70 45 52	FR551N	[OIII]	5402	2 \times 250
					FR647M	Cont.	6154	1 \times 60
					FR716N	H α	7343	2 \times 200
3C 319.0	0.1920	12 Nov 2006	15 24 05.5	+54 28 15	FR551N	[OIII]	5602	2 \times 250
					FR647M	Cont.	6556	1 \times 60
					FR782N	H α	7823	2 \times 200
3C 388.0	0.0917	29 Dec 2006	18 44 02.4	+45 33 30	FR601N	[OIII]	5968	2 \times 250
					FR647M	Cont.	6004	1 \times 60
					FR716N	H α	7164	2 \times 200
3C 390.3	0.0561	30 Dec 2006	18 42 09.0	+79 46 17	FR551N	[OIII]	5466	2 \times 250
					FR647M	Cont.	5808	1 \times 60
					FR716N	H α	6930	2 \times 200
					FR551N	[OIII]	5287	2 \times 250

NOTE. — The 19 3CR radio galaxies observed as part of the *HST* Cycle 15 SNAP program 10882 (PI: Sparks), listed by source name in ascending order. (1) 3CR source name; (2) redshift; (3) observation date; (4) right ascension (J2000.0, in hours, minutes, and seconds); (5) declination (J2000.0, in degrees, arcminutes, and arcseconds); (6) ACS ramp filters used, listed for the 60 s continuum, the 400 s H α , and the 500 s [OIII] λ 5007 observations, respectively; (7) Emission line (or continuum) observed, corresponding to filter configuration; (8) Redshift-adjusted Wavelength of emission line being observed, corresponding to the wavelength to which the ramp filter has been configured, with 2% bandpass for the H α and [OIII] exposures, and 9% bandpass for the continuum exposures; (9) Exposure time in seconds. The continuum images are single exposures, while the emission line observations consist of two exposures in a two-point dither pattern. See §2 for more details on the sample selection and observations for this program. Also part of this program was 3C 371, the observation of which failed due to failure of guidestar acquisition. It is therefore excluded from presentation and analysis in this paper. See Table 2 for a summary of the optical properties of the above sample, and Table 3 for a summary of its radio properties.

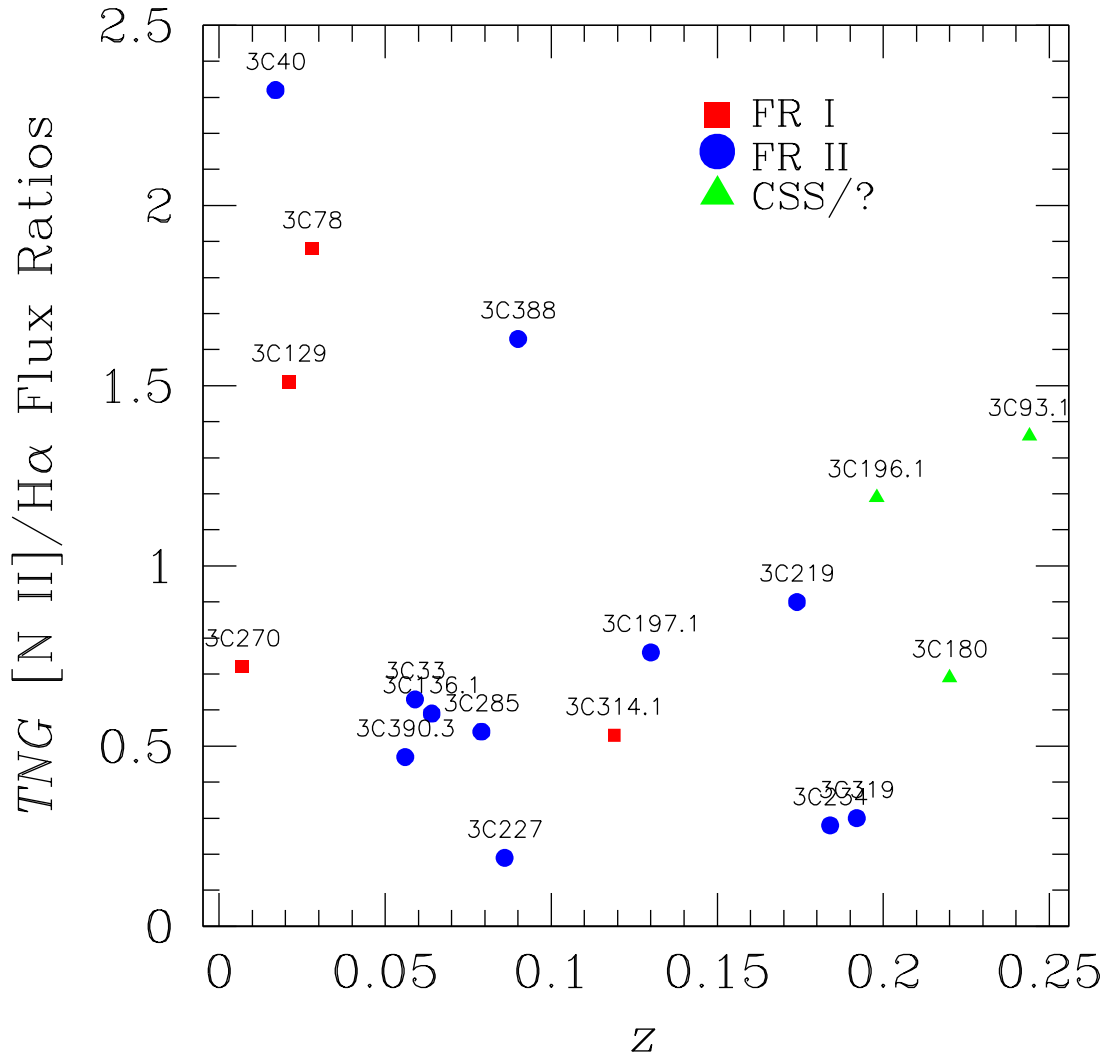


FIG. 3.— An illustrative example of the degree to which [NII] flux varies relative to $H\alpha$ among the 3CR radio galaxies discussed in this paper. Here we plot de-reddened flux ratios of the diagnostic line [NII] λ 6584 to $H\alpha$ vs. redshift. The flux ratios are from the ground-based optical spectroscopy performed by Buttiglione et al. (2009) using the Telescopio Nazionale Galileo (TNG). The results from that work show that the relative contributions of [NII] and $H\alpha$ vary widely from source-to-source, and that [NII] appears to dominate in most high-excitation galaxies (HEG, see Table 2). Red squares represent the four FR Is in our sample, while blue circles are FR IIs and green triangles represent those objects exhibiting a CSS or unclassified radio morphology. 3C 132 is excluded from this plot as no TNG spectroscopy was available for this object.

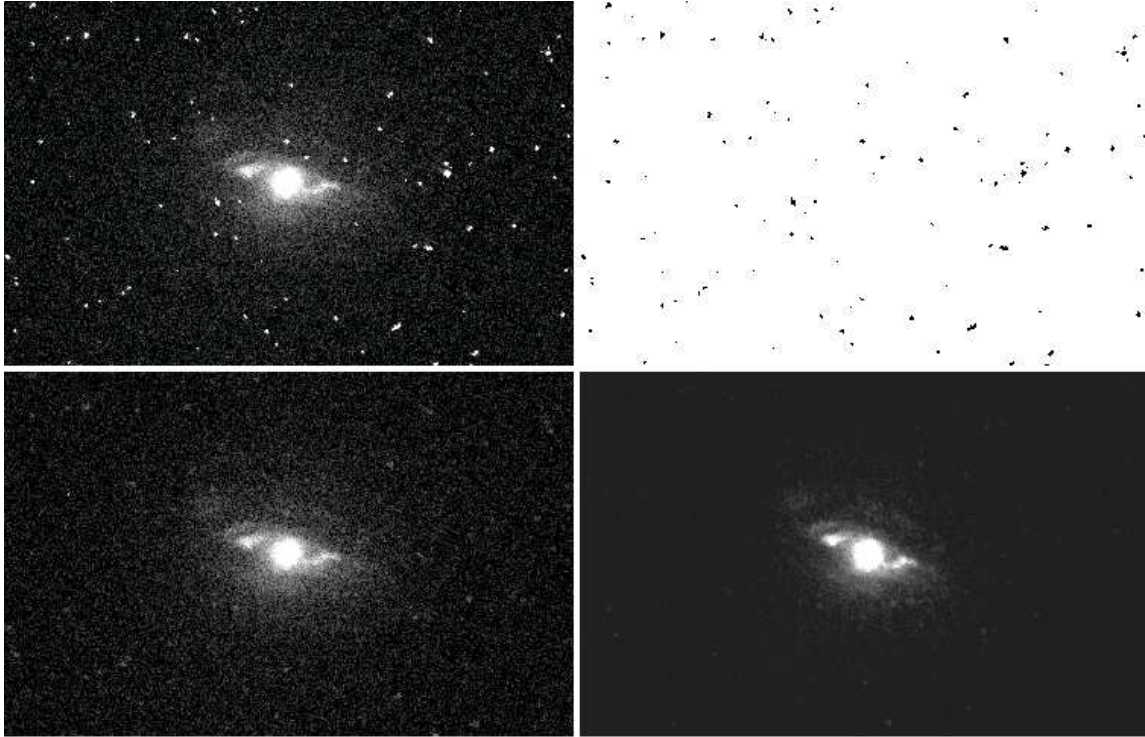


FIG. 4.— A representative example of our iterative masking process for cleaning each image of cosmic rays and hot pixels. (*Top left*) Calibrated (by `calacs`, see §3.1) single-pointing $H\alpha+[NII]$ exposure of 3C 33, one of two exposures that are combined during the `multidrizzle` process to produce a single image (as described in §3.3). (*Top right*) One of the two CR and hot pixel masks created for the exposure presented at (*Top left*) by the `cosmicrays` routine, as discussed in §3.2. This mask was used to specify locations on the exposure in (*Top left*) at which to linearly interpolate across bad pixel regions by neighboring good pixels, as described in §3.2. In this representation, the bad pixels are displayed as black. (*Bottom left*) The same exposure as in (*Top left*) after two iterations of the CR/hot pixel cleaning process with the bad pixel masks. (*Bottom right*) The combined drizzled $H\alpha+[NII]$ image of 3C 33, using the two dithered exposures (one of which is presented at *Bottom left*) that have been cleaned prior to the use of `multidrizzle` by our iterative masking process. These images are significantly cleaner than those provided by the OTFR pipeline, particularly in the case of the single-pointing continuum images. See §3 for more information.

In selecting the appropriate new flat to use (in lieu of the old ground flats used by the OTFR pipeline) we employ the same strategy that was used when the original ground flats for the ramp filters were created. That is, LRF flats are interpolated from flats for ACS narrow, medium, and broad-band (i.e. non LRF) filters that correspond most closely with the redshift-adjusted wavelength of the emission line (or continuum) being imaged. The minor difference in central wavelength, throughput, and bandwidth of these (non LRF) filters corresponds to negligible differences in their corresponding flat fields (less than the $\sim 7\%$ uncertainty introduced in using the old ground LRF flats).

With the replacement flats chosen on a case-by-case basis and the image headers updated to reflect these changes, the `calacs` routine was run for each image, producing calibrated FITS files (one for the continuum exposure, and two each for the $H\alpha+[NII]$ and $[OIII]$ exposures) that have been flat-fielded and corrected for bias, dark current, and absolute sensitivity. It is upon these calibrated images that cosmic ray and hot pixel rejection was performed, as we discuss in the following section.

3.2. Cosmic ray and hot pixel rejection

The NOAO IRAF task `cosmicrays` (`noao.imred.crutil`) was run on copies of the science frames of each calibrated exposure (one for the continuum image, two each for the $H\alpha+[NII]$ and $[OIII]$ images) to identify CRs and hot pixels. The routine identifies cosmic ray events by a detection algorithm based on a mean flux comparison within a specified detection window. A pixel within this

window whose value is higher than a user-specified threshold dependent upon the mean value of its neighbors is considered “bad”, and flagged for cleaning by the routine. Once the list of cosmic ray and hot pixel candidates is established over the whole image, `cosmicrays` replaces flagged pixels with the mean value of its four neighbors. A “cleaned” output file is then generated. We were careful to ensure that `cosmicrays` did not mis-identify real features (particularly galaxy nuclei or other physical, bright features) as CRs or hot pixels. The routine’s parameters were adjusted if this was the case.

The “cleaned” output from `cosmicrays` is insufficient for our needs, as the routine will often simply “dull” the CR rather than truly replace it. This is because `cosmicrays` flags pixels within a detection window that often contains neighboring pixels that are also affected by the CR (and are therefore far brighter than the true background). In the worst instances, depending on the parameters that are chosen, `cosmicrays` can sometimes *reconstruct* the very CR it was attempting to mask.

Therefore, we utilized the “cleaned” output from `cosmicrays` only as an intermediate step towards the creation of a bad pixel mask for each exposure. To that end, we divided the original, uncleaned copy of the calibrated science frame with the “cleaned” output from `cosmicrays`. The divided image was then examined by eye, and blinked with the uncleaned frame so as to qualitatively assess the success of `cosmicrays` in identifying offending pixels. The bad pixel mask was then created from the divided image, in which pixels whose values were above a specified threshold

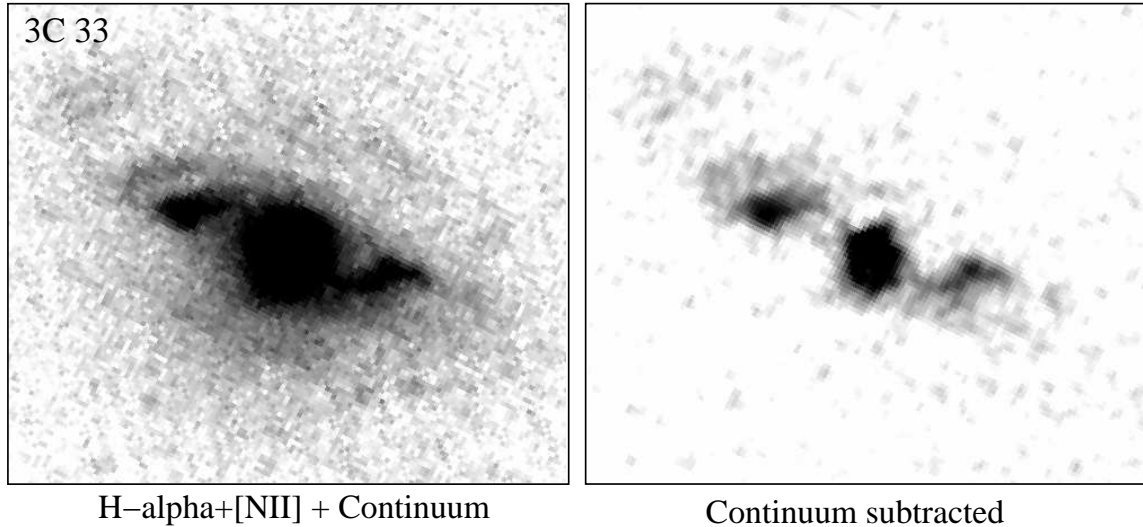


FIG. 5.— A “before and after” example result from our continuum subtraction process. (a) Reduced FR716N $H\alpha$ + $[NII]$ image of 3C 33, contaminated by galaxy continuum. (b) The same image, with galaxy continuum subtracted via the method discussed in §3.5

dictated those that were to be masked in the uncleaned image. This threshold was decided qualitatively for each image based on our assessment of the success of `cosmicrays` in distinguishing truly bad pixels from real features. Often, accepting every flagged pixel from the divided image into the final mask would result in masking healthy pixels on the galaxy itself. If this appeared to be the case, the “allowance threshold” was set *above* the values of the incorrectly flagged pixels in the divided image, so that they were not made part of the final mask. We paid particular attention to flagged pixels within the immediate vicinity of the target galaxy, and ensured on a case-by-case basis that the pixels being masked were indeed CR events or hot pixels and not real features in the galaxy. This was accomplished through blinking individual exposures or by comparing the continuum image to archival *HST* data from e.g. WFPC2 in the few cases where the correct choice was not obvious.

The mask was then used with the `fixpix` task to linearly interpolate values for masked pixels based on those of their nearest unmasked neighbors. While this is in effect similar to the procedure employed by `cosmicrays`, it is more robust in that `fixpix` is better able to replace a CR event with pixels generally consistent with that of the true background. `cosmicrays`, on the other hand, will often simply “dull” the CR rather than truly replace it, as it flags pixels within a detection window that often contains neighboring pixels affected by the CR (and are therefore far brighter than the true background). Moreover, the masking process allows the user to check at each step that no real feature on the galaxy is erroneously altered. This process was repeated several times (typically three times) for *each* calibrated science frame (one continuum exposure, two $H\alpha$ + $[NII]$ frames, and two $[OIII]$ frames). At each iteration in the process we varied the detection thresholds in `cosmicrays`, as well as the parameters associated with creating the subsequent mask, in order to ensure that all CRs and hot pixels were ultimately identified and cleaned. In Fig. 4 we provide a representative example of the steps in our cosmic ray and hot pixel rejection strategy. The upper-left and lower-right panels in the figure serve as a “before and after” comparison.

In two cases (3C 33 and 3C 78) a large CR event landed directly on or near to the target galaxy image in the single

pointing continuum exposure. In these cases we masked the CR while taking care to affect the galaxy light distribution as little as possible. Inevitably, some error due to pixel value interpolation remains on the final reduced images (as the continuum exposure is used for both $H\alpha$ + $[NII]$ and $[OIII]$ in the continuum subtraction process, described in §3.4). However, while this error is difficult to characterize it is unlikely that it has a significant effect on the ultimate science value of the data, both for morphological studies of the emission-line region and for e.g. flux measurements.

3.3. Multidrizzle

The calibrated, cleaned data were passed through the `multidrizzle` routine with the default parameters. The task calculates and subtracts a background sky value for each exposure, searches for additional bad pixels not already flagged in the data quality array, and drizzles the two exposures into outputs that are shifted and registered with respect to one another. From these drizzled exposures a median image is created, which is then compared with original input images so as to reject the (very few) CRs not already cleaned in our previous CR rejection process, as we describe in the section above. More information on the specifics of `multidrizzle` can be found in Koekemoer et al. (2002). Final output images were left unrotated with respect to north to avoid pixel interpolation errors that might add uncertainty to our continuum subtraction and flux estimation strategies, which we describe in the sections below.

3.4. Image Alignment

To facilitate continuum subtraction it was first necessary to align the continuum exposures with their corresponding drizzled emission line images to ensure registration down to a fraction of a pixel. A first pass registration was made by the world coordinate system (WCS) to achieve rough alignment of the continuum image with its companion line emission data. Subsequently, fractional shifts and rotations were manually applied using foreground stars and features on the galaxy as alignment aides (with the added help of the task `imalign`). Initial image registration was already well established for 8 of the 19 galaxies in our sample as their observations were carried out using the same guide stars in all (con-

TABLE 2
OPTICAL PROPERTIES

Source (1)	H α Line Flux ($\times 10^{-15}$ erg s $^{-1}$ cm $^{-2}$) (2)	[OIII] Line Flux ($\times 10^{-15}$ erg s $^{-1}$ cm $^{-2}$) (3)	log $L_{\text{H}\alpha}$ (erg s $^{-1}$) (4)	log $L_{\text{[OIII]}}$ (erg s $^{-1}$) (5)	Ionization Class ^{a,b} (6)	L.A.S $_{\text{H}\alpha}$ (kpc) (7)
3C 33.0	0.428	1.58	39.5255	40.0927	HEG	5.142
3C 40.0	1.69	1.66	39.0232	39.0154	LEG	1.259
3C 78.0	2.18	2.15	39.5719	39.5659	...	2.208
3C 93.1	0.103	0.070	40.2147	40.0470	...	3.806
3C 129.0	0.12	0.087	38.0598	37.9201	...	0.243
3C 132.0	0.079	0.081	39.9738	39.9847	LEG	9.77
3C 136.1	0.205	0.123	39.2786	39.0567	...	2.64
3C 180.0	0.228	0.488	40.4605	40.7910	HEG	16.78
3C 196.1	0.149	0.136	40.1756	40.1360	LEG	8.72
3C 197.1	0.121	0.091	39.6925	39.5687	HEG	3.04
3C 219.0	0.148	0.143	40.0509	40.0360	BLRG	1.90
3C 227.0	1.931	0.569	40.5184	39.9878	HEG ^c	21.76
3C 234.0	0.941	2.050	40.9068	41.2449	BLRG	6.47
3C 270.0	1.91	2.10	38.3014	38.3425	...	0.63
3C 285.0	0.433	0.711	39.7925	40.0079	HEG	6.49
3C 314.1	0.016	0.070	38.7325	39.6781	...	3.13
3C 319.0	0.027	0.016	39.4047	39.4820	LEG	6.79
3C 388.0	0.056	0.366	39.0220	40.1419	LEG	1.98
3C 390.3	11.5	1.94	40.9081	40.4398	BLRG	2.97

REFERENCES. — (a) Jackson & Rawlings (1997), (b) Buttiglione et al. (2009), (c) Prieto (1993)

NOTE. — (1) 3CR source name; (2) measured H α (6563 Å) line flux in erg s $^{-1}$ cm $^{-2}$; (3) total measured [OIII] (5007 Å) line flux in erg s $^{-1}$ cm $^{-2}$; (4) total H α luminosity in erg s $^{-1}$ and (5) total [OIII] luminosity in erg s $^{-1}$ (fluxes converted to luminosity using $H_0 = 71$ km s $^{-1}$ Mpc $^{-1}$, $\Omega_M = 0.27$, and $\Omega_\Lambda = 0.73$); (6) Source classification of host (FR I = Fanaroff-Riley class I radio galaxy, QSO = quasar, BLRG = broad line radio galaxy, HEG = high-excitation FR II galaxy, LEG = low-excitation FR II galaxy, per the conventions in Jackson & Rawlings 1997); (7) largest measured angular size of line-emitting region (noted emission line in parentheses note the line for which the observed NLR appears largest, both lines will be listed if the NLRs cover approximately the same physical extent in both lines).

tinuum, H α + [NII], and [OIII]) exposures. The remaining 11 observations included small slews of *HST* to allow for proper placement of the galaxy image on the WFC chip (necessary to image at the desired LRF wavelength). In these cases guide star acquisition was required between exposures. Registration for these 11 targets was therefore not initially ideal, and great care was taken to ensure proper alignment through manually applied shifts and rotations. After the appropriate shifts and rotations were applied, the WCS systems on the images were registered with respect to one another so as to enable proper WCS alignment when viewing the images.

3.5. Continuum subtraction

Here we describe the steps taken to produce H α + [NII] and [OIII] line emission images that are effectively free from contamination by continuum light from the galaxy. The aligned images were multiplied by their exposure times to set pixel values (in electrons per second for drizzled ACS images) to total electrons. The continuum image was then scaled by a factor determined for each image on a case-by-case basis. Initially, this factor was roughly estimated using the *synphot* synthetic photometry package (specifically *calcphot*) in IRAF. The *calcphot* models served as a qualitative guide in roughly establishing the scaling factor, which was later refined iteratively through a trial and error process that involved scaling and subtracting the continuum image from the line emission image, and examining residual pixel values on the resultant image in regions known to be dominated by continuum emission on the original unsubtracted data. The process was repeated until these regions possessed a mode pixel value very close to the background level (which was effectively zero, after the multidrizzle process). Ultimately, the above strategies were employed in both qualitative and quantitative ways on a case-by-case basis for each image, ensuring that the final subtracted image could be confidently consid-

ered as “pure” line emission within the error established by the absolute photometry for this dataset. In Fig. 5 we provide a representative “before and after” comparison in the case of continuum subtraction for 3C 33.

3.6. Emission line luminosity measurements

For each H α + [NII] and [OIII] image we have measured the total flux from all detected line emission in the galaxy’s central regions. Emission-line fluxes were measured from the continuum-subtracted images using the *apphot* routines in IRAF. We adopted an “all the flux you see” approach when establishing the size of the aperture with which the photometric measurement was performed. In this way, we measure “total” flux as opposed to flux through an aperture that is the same across the the entire dataset.

For consistency, we defined a “source region” by heavily smoothing a copy of each emission line image with a Gaussian kernel set to an arbitrarily large sigma. The aperture for the measurement was then set to the radius corresponding to a reasonable contour in the smoothed image enclosing all detected line emission from the galaxy. We also defined an outer boundary beyond which the image may be non-monochromatic (due to the ramp filters, see §2 for an explanation). The region between the “source region” and the outer boundary defined the area in which the H α + [NII] and [OIII] background level was measured.

With these regions defined using the smoothed image, the corresponding regions on the original continuum-subtracted images were identified. The image was then examined to establish the standard deviation of background, and the pixel values were thresholded to a value of order one sigma above the background level, corresponding to ~ 0.01 electrons per second. Counts above this threshold were considered signal and were counted in the photometric summation of flux values, while pixels below this threshold were read as zero and

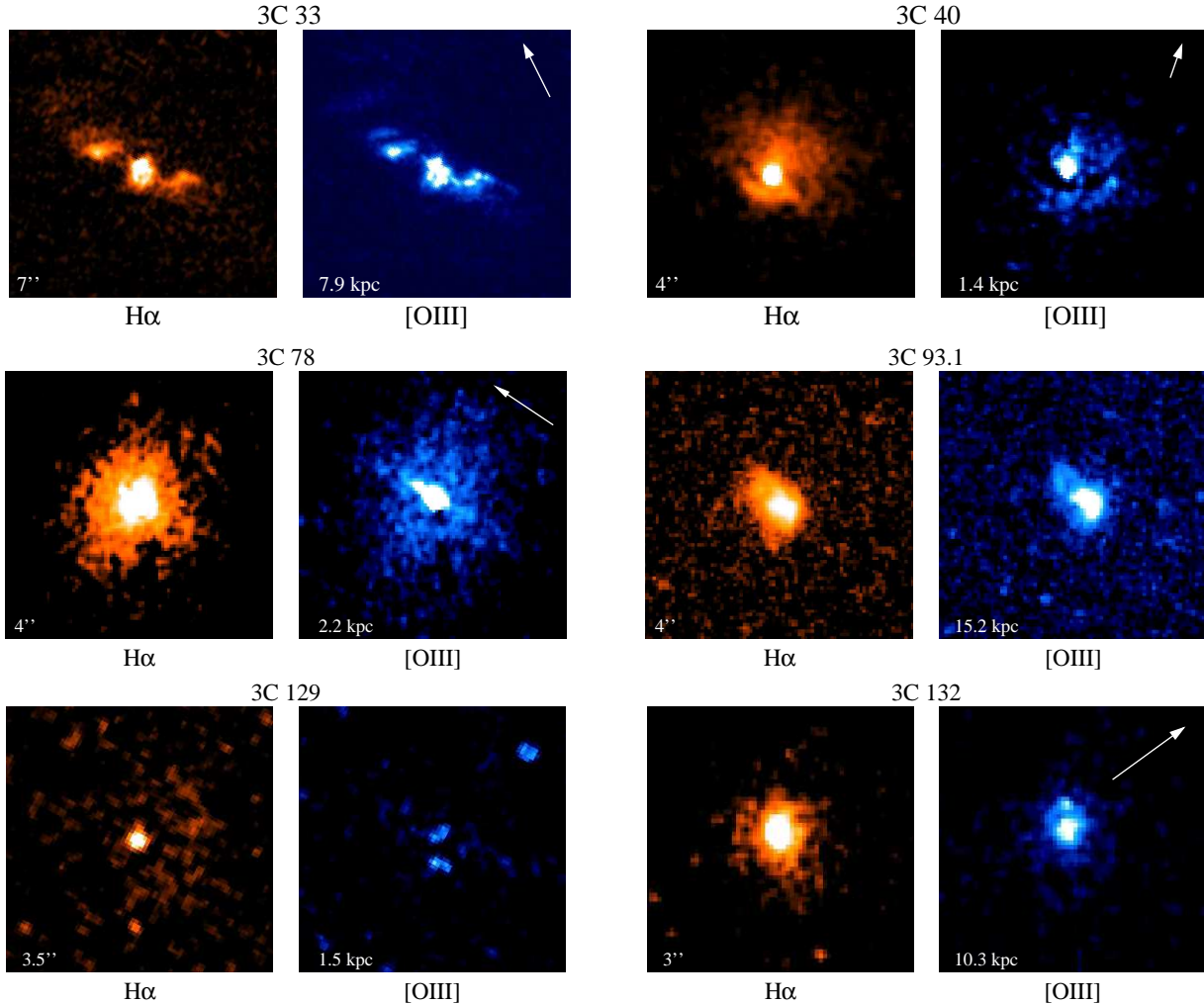


FIG. 6.— *HST/ACS* narrow-band images of the $H\alpha+[NII]$ (left panel, in red) and $[OIII]$ (right panel, in blue) line emitting regions in our sample of radio galaxies from the 3CR catalog. Contribution from continuum has been subtracted using a strategy discussed in §3. In the bottom left corner of the left (right) panel we indicate the size of the field of view in arcsec (kpc). Both images are aligned, with East left and North up. The arrows in the upper right corner of some panels indicate the projected orientation of the radio jet axis on the sky, estimated from high resolution VLA radio maps (where available). Galaxies are listed in ascending order by 3CR name. See Table 1 for more details on these observations, and §4 for descriptions of the emission line features of each target.

were not counted.

We summed counts above the pre-defined threshold within the source region (aperture), and then subtracted the estimated background measured similarly within the intermediate region (exterior to the source region but interior to the outer boundary). Photometric conversion was then applied by scaling the residual (source minus background) value by the inverse sensitivity (the PHOTFLAM keyword), converting the value from electrons per second to flux units in $\text{erg cm}^{-2} \text{s}^{-1} \text{\AA}^{-1}$. Flux measurements were made on unrotated images to avoid pixel interpolation errors. Emission line flux values were converted to luminosities via the luminosity distance. Non-rotated images were used for flux calibration to minimize pixel interpolation errors. Ultimately, the calibrations allow us to measure emission line flux with an uncertainty of $\sim 15\%$.

4. RESULTS & DISCUSSION

In Figs. 6 - 8 we present the continuum-free line emission images listed by ascending 3C number. $H\alpha+[NII]$ images are shown to the left and are presented in orange and $[OIII]$ images are shown to the right in blue. Where possible we have estimated the projected orientation of the radio jet axis

on the sky from high spatial resolution archival Very Large Array (VLA) radio maps retrieved from the NASA/IPAC Extragalactic Database (NED¹³), indicated by an arrow in the top right corner of the galaxy's $[OIII]$ image. This orientation was *qualitatively* estimated from the apparent inner jet axis for FR I radio galaxies, and along the hotspot-to-hotspot axis for FR II radio galaxies. See Table 3 for a summary of the radio properties for objects in the sample. In instances where the figure does not display an estimate for the radio jet orientation, data was either not readily available, was of insufficient resolution to make a confident estimate, or was cospatial with the source on galactic scales (i.e. morphologically similar to CSS sources).

4.1. Description of individual sources

In the subsections below we discuss the observed morphology of the high surface brightness $H\alpha+[NII]$ and $[OIII]$ line emission detected in each galaxy. Objects are listed in ascending order by the name of the source. For information relating to the observations of each of the below galaxies, see Table 1. For quantitative data regarding the optical and radio

¹³ <http://nedwww.ipac.caltech.edu/>

properties of each object, see Tables 2 and 3, respectively. All images discussed below are presented in Figs. 6, 7, and 8.

4.1.1. *3C 33*; $z = 0.059$

Extended regions of high surface brightness line emission are seen in both the $H\alpha+[NII]$ and $[OIII]$ images. The low- and high-excitation regions trace a general “integral sign” shape extending ~ 5 kpc and oriented NE to SW. In both images a fainter, detached shell of low- and high-excitation emission is observed NE of the main “integral sign” feature. The $[OIII]$ features more obviously clumpy, brighter hotspots along the lane of emission and near the nucleus than does the $H\alpha+[NII]$ image. Long slit spectroscopy of the extended line emission obtained by Simkin (1979) and Heckman et al. (1985) suggested that the line emitting gas is rotating along an axis oriented at a position angle (P.A.) of $\sim 19^\circ$ with respect to the FR II radio jet axis. (Fig. 6).

4.1.2. *3C 40*; $z = 0.017$

A dusty disk on 100 pc scales is seen in both $H\alpha+[NII]$ and $[OIII]$ images, marked by the absence of emission along a circumnuclear rim that is more prominent in the $[OIII]$ image than it is in $H\alpha+[NII]$. Low- and high-excitation line emission is seen tracing the edges of the disk on the southern side, while $[OIII]$ emission on the northern side of the disk appears less extensively distributed. The band marking the disk is not continuous, rather in both images it is interrupted by low-surface brightness line-emission apparently connecting the southern and northern sides of the disk in the same general location. Note that the apparent major axis of the disk appears roughly orthogonally oriented with respect to the FR II radio jet axis. (Fig. 6).

4.1.3. *3C 78*; $z = 0.028$

An optical jet is seen in both $H\alpha+[NII]$ and $[OIII]$ emission to extend from the core in a northeasterly direction (projected on the sky). The bright, unresolved nucleus in both images is surrounded by a generally isotropic region of narrow-line emitting gas in both $H\alpha+[NII]$ and $[OIII]$. Sparks et al. (2000) noted the presence of a face-on dusty nuclear disk in this FR I radio galaxy. Both distributions appear slightly more extended in the plane perpendicular to the optical synchrotron radio jet axis described by Sparks et al. (1995). Perlman et al. (2006) notes the presence of an emission line knot cospatial with the radio jet axis. That we apparently detect both high- and low-excitation emission along the jet axis may be an important result, and is worthy of future study. (Fig. 6).

4.1.4. *3C 93.1*; $z = 0.244$

A compact distribution of narrow-line emitting gas is seen surrounding the nucleus and extended ~ 3.8 kpc primarily towards the NE. The lopsided morphology observed in both the $H\alpha+[NII]$ and $[OIII]$ emitting gas is evidence of the presence of an anisotropic nuclear ionizing radiation field. *3C 93.1* is a CSS source. (Fig. 6).

4.1.5. *3C 129*; $z = 0.021$

Narrow-line emission associated with *3C 129* is only marginally detected in both filter configurations. Compact $H\alpha+[NII]$ emission with very low surface brightness is observed to be cospatial with the nucleus. Conversely, the nucleus is not detected in the $[OIII]$ image, where instead only very faint extended emission that appears to be associated with the nucleus extends $1''$ to the north and south. *3C 129* is one of the four FR I radio galaxies in our sample (Fig. 6).

4.1.6. *3C 132*; $z = 0.214$

A bright nucleus surrounded by fainter, more diffuse emission is observed in both $H\alpha+[NII]$ and $[OIII]$ images. The nucleus appears fainter in $[OIII]$ and what appears to be a faint “hotspot” is located directly to the north of the nucleus. (Fig. 6).

4.1.7. *3C 136.1*; $z = 0.064$

In $H\alpha+[NII]$, an elongated nucleus is seen with major axis oriented north-south on the sky. Faint, disjoint distributions of narrow-line gas surround the nucleus in two filamentary plumes extending from the core along a N-S axis roughly perpendicular to the FR II radio jet axis. Clumpy patches of disparate, low-surface brightness emission are observed at radii of $\sim 1''$. In $[OIII]$ there is an apparent double nucleus with hotspots more clearly separated than in the $H\alpha+[NII]$ image. The north-south filaments seen in $H\alpha+[NII]$ are not detected in $[OIII]$. (Fig. 7).

4.1.8. *3C 180*; $z = 0.220$

A bi-conical series of shells is observed in both $H\alpha+[NII]$ and $[OIII]$, reminiscent of other bi-conical NLR morphologies observed in some Seyfert II galaxies (e.g., Mrk 3, Mrk 573, NGC 5252, Capetti et al. 1999). At both low- and high-excitation we observe a bright, lopsided emission region cospatial with the nucleus. Fainter “plume-like” features extend from both the northern and southern extremities of the extended core of emission. The bi-conical series of shells of emission extends ~ 8 kpc to both the NE and SW of the core. The abundance of optical line emitting gas along a preferred axis suggests the presence of a highly anisotropic ionizing radiation field. *3C 180* lacks a Fanaroff-Riley classification, and we are unable to characterize the morphology of its radio source in any meaningful way given the available data. McCarthy et al. (1995) note that *3C 180* resides in a cluster. (Fig. 7).

4.1.9. *3C 196.1*; $z = 0.198$

A high surface brightness lane of $H\alpha+[NII]$ emission “snakes” NE from the bright elongated core, reminiscent of a “tadpole” shape. $H\alpha+[NII]$ emission is also observed extending from the core along an axis perpendicular to the axis of elongation of the “tadpole”-shaped distribution of ionized gas. In the $[OIII]$, high excitation emission is observed in two localized hotspots cospatial with the elongated bright core seen in $H\alpha+[NII]$, and the “tadpole” structure is not detected, nor is the emission along the perpendicular axis. (Fig. 7).

4.1.10. *3C 197.1*; $z = 0.13$

Bright, unresolved nuclei are seen in both images, surrounded on all sides by a fainter distribution of line-emitting gas. The nucleus appears larger in $H\alpha+[NII]$ than it does in $[OIII]$. (Fig. 7).

4.1.11. *3C 219*; $z = 0.174$

Compact emission is seen in both bands, as is faint, diffuse emission surrounding the unresolved source at the center. (Fig. 7).

4.1.12. *3C 227*; $z = 0.086$

Compact emission cospatial with the galaxy’s nucleus is seen at both low- and high- excitation. In $[OIII]$ we observe

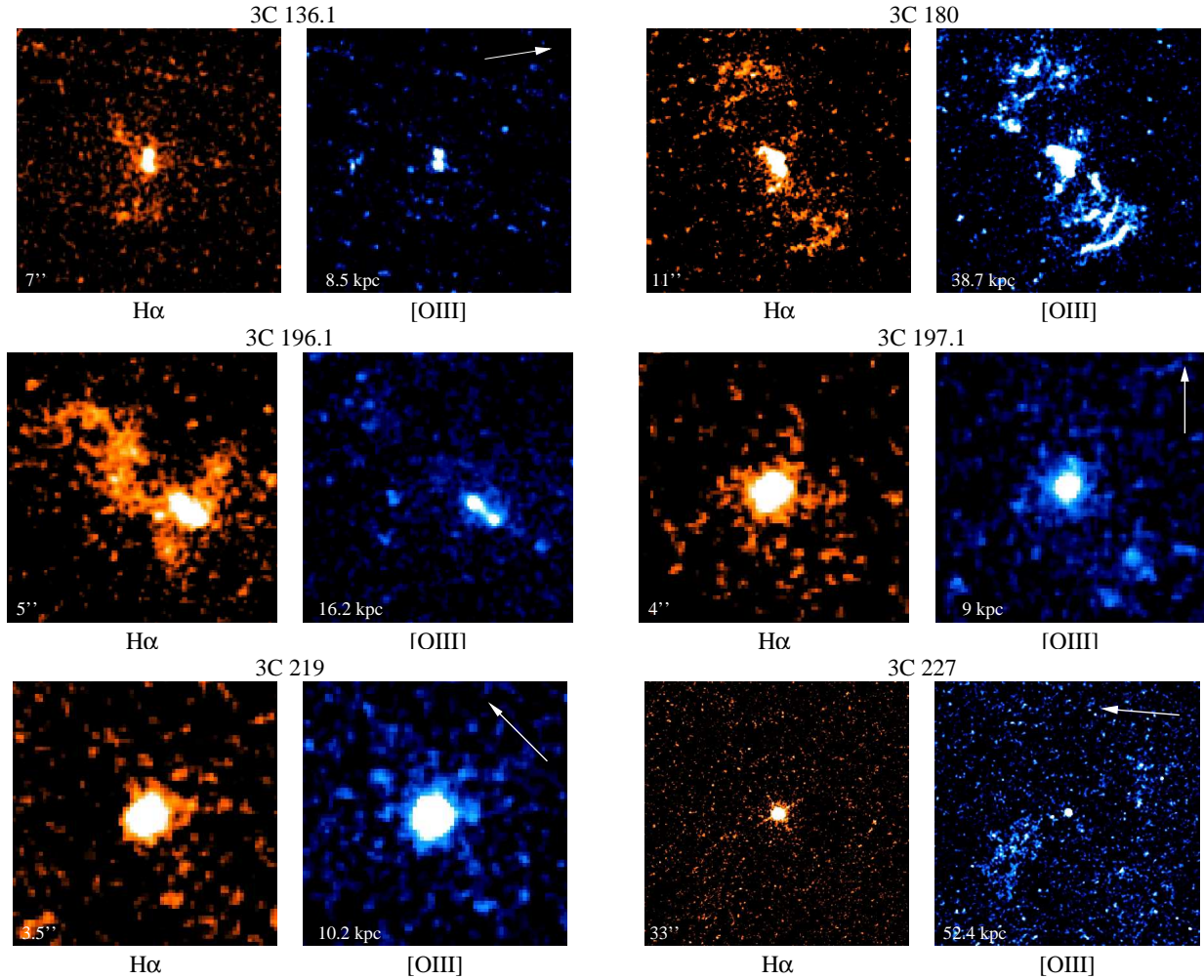


FIG. 7.— Same as Fig. 6. East is left, North is up. Note that panels labeled “H α ” actually show H α +NII emission.

an extremely large arm of emission extending ~ 20 kpc, representing by far the largest distribution of line-emitting gas in our sample. The large structure is oriented along an axis roughly perpendicular to that of the FR II radio jet. Prieto (1993) studies this object in great detail. (Fig. 7).

4.1.13. 3C 234; $z = 0.184$

The prominent tidal arm described by Carleton et al. (1984) is seen in high surface brightness H α +NII and [OIII] emission. To the east is the bright quasar-like nucleus of the galaxy, and in both images a bright feature is seen extending $0.5''$ from its northwestern edge. The overall elongation of the emission line region, including the tidal arm, is in a projected orientation that is roughly parallel with that of the radio jet axis on large scales. (Fig. 8).

4.1.14. 3C 270; $z = 0.0077$

The ~ 120 pc dusty disk originally studied by Jaffe et al. (1993) is notably absent of emission in both H α +NII and [OIII], though there remains some H α +NII emission along the inner regions of the disk. The disk is largely edge-on with respect to the line of sight though is inclined such that the western side of the disk “faces” the observer slightly. Note that the western half of the galaxy is noticeably brighter than the eastern half. Cones of high surface brightness H α +NII emission are seen extending from the unresolved

nucleus from both sides of the disk, and are elongated along the direction of the jet (east-west on the sky, and nearly perpendicular to the major axis of the dusty disk). Nuclear [OIII] emission is also seen extending from both sides of the disk, though seems to be largely absent on the disk itself. (Fig. 8).

4.1.15. 3C 285; $z = 0.079$

A complex, filamentary system of dust lanes bisects the nuclear region of the galaxy in a northeasterly direction and perpendicular to the line of sight. The extinction associated with the predominant lane in this system is seen in the H α +NII, where we observe an extended region of high surface brightness emission with complex morphology. A bright, dense column of line-emission extends $\sim 1''$ northward from the nucleus at the center of the image. Slightly to the southeast a small, bright “integral sign” feature is seen in general alignment with the large dense column. Both of these features are surrounded by fainter narrow-line emitting gas arranged in filamentary plumes as well as clumpy patches. In the [OIII] image we observe a dramatically different morphology than is apparent from the H α +NII. A high surface brightness lane of emission “snakes” westward from the center of the galaxy to form a disjoint “W” shape. The nucleus of the galaxy, such as it is, is not discernible from the image. Bright patches of emission populate the prominent filament at regular intervals along its length. A region of particularly high surface bright-

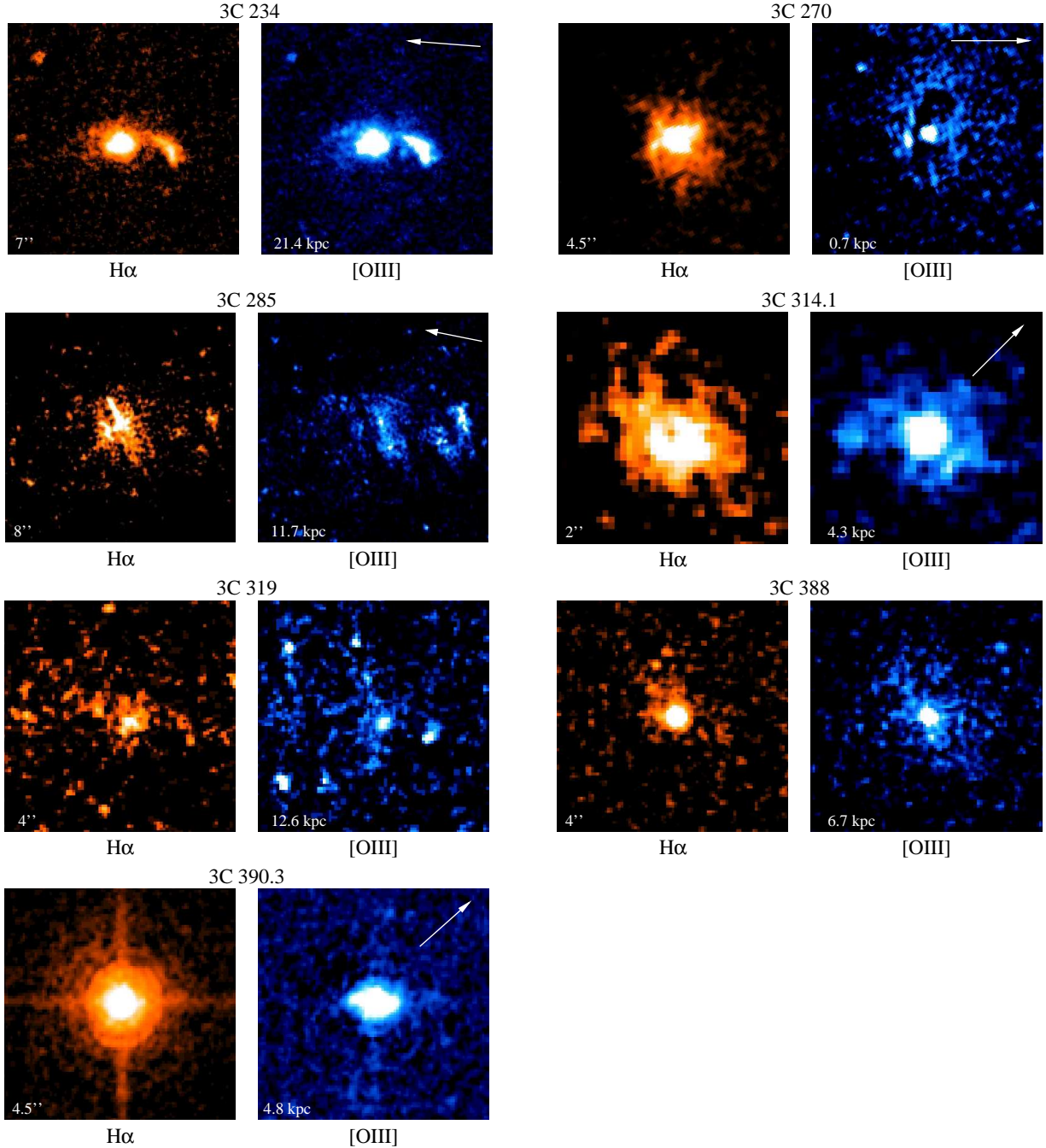


FIG. 8.— Same as Fig. 6. East is left, North is up. Note that panels labeled “H α ” actually show H α +NII emission.

ness emission is noted at its westernmost extremity. (Fig. 8).

4.1.16. 3C 314.1; $z = 0.119$

Diffuse H α +NII emission is distributed in a complex morphology, while the [OIII] emission is decidedly more compact, albeit with faint, wispy plumes extending from the nucleus and slightly toward the southwest. (Fig. 8).

4.1.17. 3C 319; $z = 0.192$

Very faint line emission is detected in both images, distributed in a diffuse, complex morphology at extended distances from the nucleus. The [OIII] is decidedly more compact than is the H α +NII. (Fig. 8).

4.1.18. 3C 388; $z = 0.092$

A bright unresolved nucleus is seen in both images. Small, low surface brightness “plumes” can be seen extending toward a northeasterly direction in the H α +NII, while a more prominent conical feature is seen on the southwestern side of the nucleus in the [OIII] image. (Fig. 8).

4.1.19. 3C 390.3; $z = 0.056$

Very bright H α +NII emission dominates the image from the unresolved nucleus. The noticeably rhomboidal shape of the nucleus in the [OIII] is likely a result of the diffraction spikes seen in both images. (Fig. 8).

4.2. Discussion: correlations

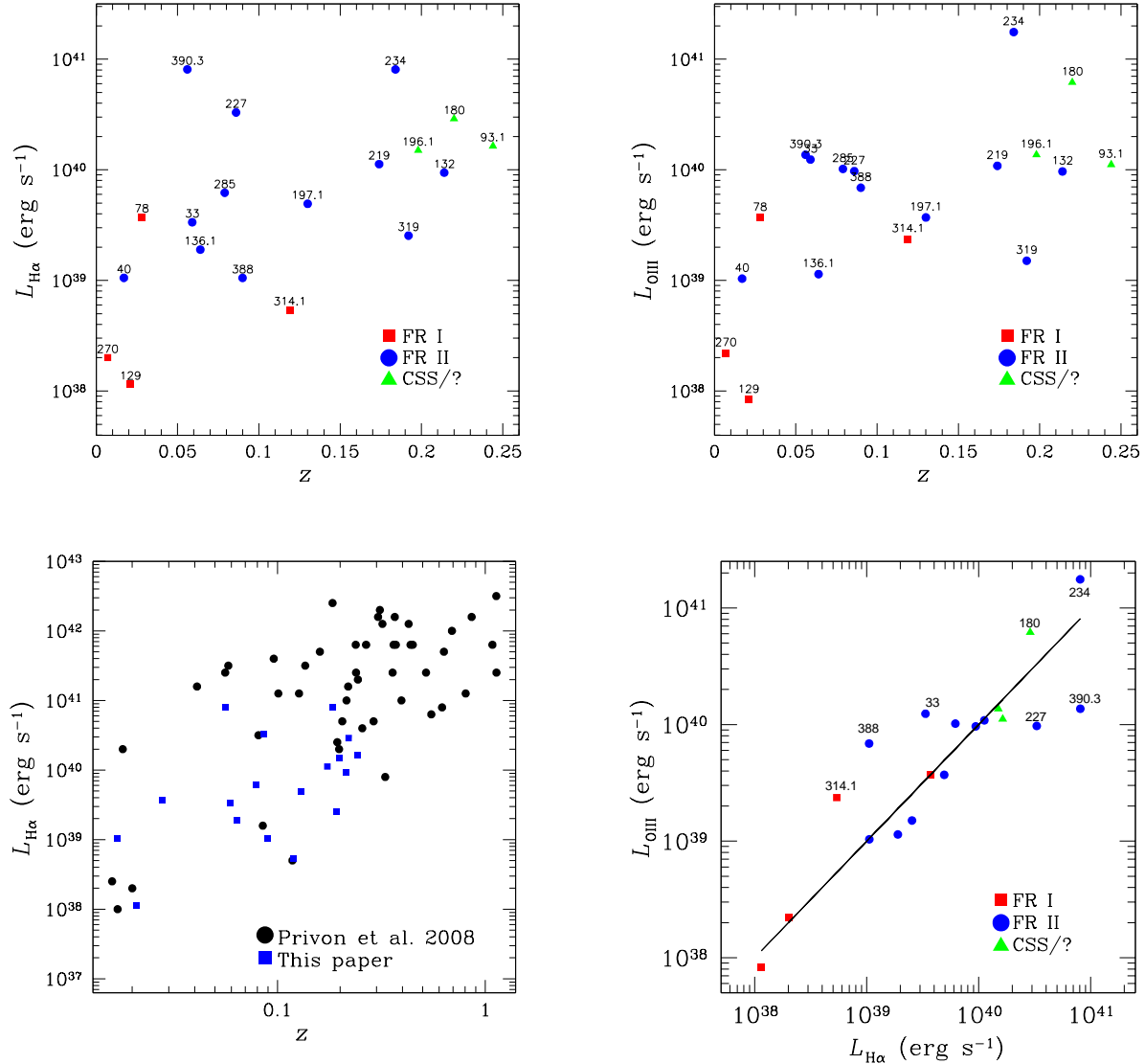


FIG. 9.— (Top left) Measured $H\alpha$ + $[NII]$ luminosity (in erg s⁻¹) vs. redshift for the 19 galaxies in our sample. Red squares represent the four FR Is in our sample, while blue circles are FR IIs and green triangles represent those objects exhibiting a CSS or unclassified radio morphology (i.e., 3C 180, see §4.1.8 for details). See §3 for a details concerning our photometry strategy. (Top right) Measured $[OIII]$ luminosities vs. redshift, using the same symbol definitions as in (top right). (Bottom left) The measured $H\alpha$ + $[NII]$ luminosities from our sample (plotted in blue squares) vs. redshift, overplotted with the *measured* and *extrapolated* $H\alpha$ + $[NII]$ luminosities for the sample of 3CR radio galaxies from Privon et al. (2008). The slightly larger scatter observed in the Privon et al. (2008) data reflects the fact that roughly 50% of their $H\alpha$ + $[NII]$ luminosities have been estimated from measured $[OIII]$ luminosities using ratios found in the literature. In general, however, our galaxies follow a redshift-luminosity correlation roughly consistent with that found for a higher redshift subset of the 3CR from Privon et al. (2008). See §4.2 for a discussion. (Bottom right) The measured $[OIII]$ luminosities vs. the measured $H\alpha$ + $[NII]$ luminosities for the objects in our sample. Those galaxies lying above the black diagonal line (tracing $L_{[OIII]} = L_{H\alpha}$) have $[OIII]$ luminosities greater than their $H\alpha$ + $[NII]$ luminosities, and vice-versa. For a discussion on the implications of these emission line luminosity ratios, see §4.2.

Below we discuss significant correlations, consistent with the results of previous related studies, that are apparent in our data. In §4.3 we discuss the physical interpretation of these observed trends, and compare our results to past literature.

4.2.1. Emission line luminosities vs. redshift

In Fig. 9a and 9b (top left and top right, respectively) we plot the measured $H\alpha$ + $[NII]$ and $[OIII]$ luminosities ($L_{H\alpha}$ and $L_{[OIII]}$) vs. redshift for the galaxies in our sample. FR I radio galaxies are plotted in red squares, while FR IIs are plotted in blue circles and the three galaxies whose radio morphologies are uncategorized are plotted in green triangles (this convention holds throughout this paper). As expected, the emission line luminosities follow a positive redshift-luminosity trend,

albeit with a greater degree of scatter than that found in the canonical $K-z$ relation for radio galaxies (where K is the NIR K -band magnitude of the elliptical radio galaxy host, see Willott et al. 2003 for a detailed study of this correlation). This higher degree of scatter is not necessarily surprising for a number of reasons, some of which we summarize below:

1. Warm optical line emitting gas in radio galaxies is naturally expected to inhabit a greater range in luminosity space than are the NIR starlight distributions of their elliptical hosts. As the stellar component of radio galaxies is believed to have formed at high redshift and evolved passively in the time since (barring other effects), a tight clustering of K -band magnitudes is expected. The amount, ionization state, and detectability

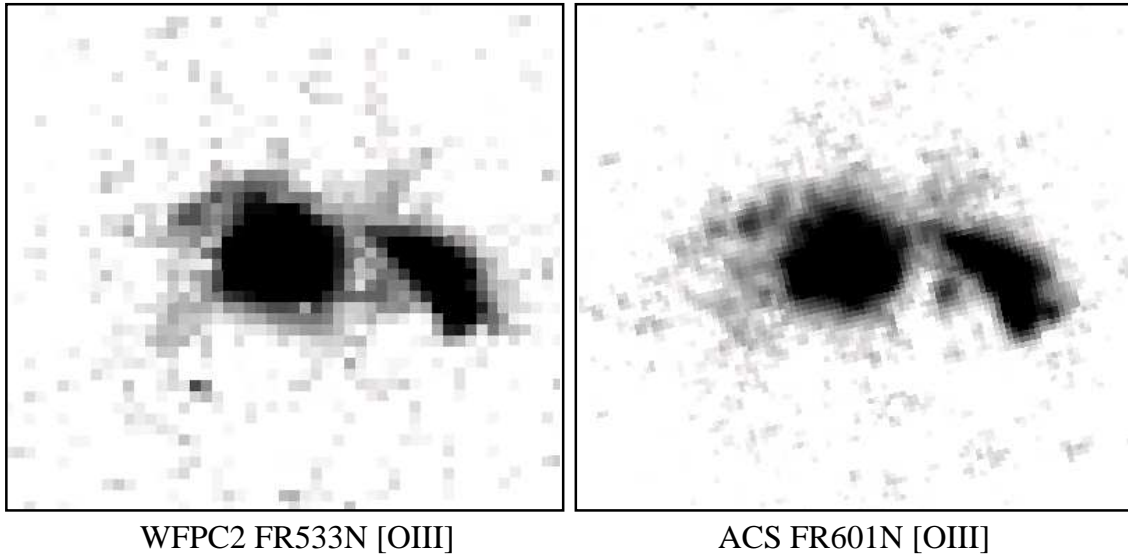


FIG. 10.— A representative comparison of data quality from the WFPC2 LRF emission line survey of 3CR radio galaxies as presented in Privon et al. (2008) in comparison with the data presented in this paper. (a) Continuum-subtracted WFPC2 FR533N 2×300 s exposure of the [OIII] emission in 3C 234; (b) continuum-subtracted ACS WFC FR601N exposure of the [OIII] emission in 3C 234, from the dataset presented in this paper. See Table 2 and §2 for details.

of gas in the nuclei of radio galaxies, however, is subject to a number of factors that greatly influence overall emission line luminosities.

2. Our sample includes low-power FR I radio galaxies, characterized by narrow-line emission, and FR II radio galaxies and QSO characterized by broad optical line emission. Broad line radio galaxies (BLRGs) generally have an optical excess, resulting in a larger contribution to emission line flux. Not surprisingly, the BLRGs in our sample (3C 33, 197.1, 219, 285, 234, & 390.3) generally inhabit the upper regions of Fig. 9a and 9b, contributing to the overall scatter.
3. These galaxies range in redshift from $0.0075 < z < 0.224$ and were observed with a variety of LRF filter configurations (see Table 2). This results in varying amounts of emission line flux loss beyond the edge of the passband, as well as contamination from [NII].

In Fig. 9c we plot our $H\alpha + [NII]$ luminosities in blue squares vs. redshift, overplotted with the *measured* and *extrapolated* $H\alpha + [NII]$ luminosities for the sample of 3CR radio galaxies from Privon et al. (2008). The slightly larger scatter observed in the Privon data reflects the fact that roughly 50% of their $H\alpha + [NII]$ luminosities have been estimated from measured [OIII] luminosities using ratios found in the literature. In general, however, our galaxies follow a redshift-luminosity trend roughly consistent with that found for the (generally) higher redshift subset of the 3CR studied in Privon et al. (2008). See Fig. 10 for a representative and qualitative comparison of WFPC2 and ACS data quality from the Privon observations and this paper, respectively.

4.2.2. Emission line ratios

In Fig. 9d (bottom right) we plot the measured [OIII] luminosities vs. the measured $H\alpha + [NII]$ luminosities for the objects in our sample. Those galaxies lying above the black diagonal line (tracing $L_{[OIII]} = L_{H\alpha}$) possess [OIII] luminosities greater than their $H\alpha + [NII]$ luminosities (and vice-versa). Note that, in general, $L_{H\alpha}$ and $L_{[OIII]}$ are roughly sim-

ilar across the sample, with some notable exceptions whose names we have indicated in the figure.

In future papers it will be necessary to investigate emission line ratio maps, which may carry important implications with regards to the orientation-based unification scheme of radio-loud AGN (e.g., Padovani & Urry 1992; Chiaberge 2004, and references therein). It is expected that low-excitation lines (like $H\alpha + [NII]$) are emitted further from the AGN than are higher excitation lines like [OIII], as the fraction of highly excited gas will depend on the proximity of that gas to the ionizing source, in this case the AGN (e.g., Jackson & Rawlings 1997, and references therein). This spatial dependence of $L_{[OIII]}/L_{H\alpha}$ also leads to a dependence upon the sources of obscuration present in the galaxy. In the unification model for radio galaxies, wherein FR Is are unified with BL-Lacs and FR IIs are unified as the parent population of steep spectrum QSO, we expect low-excitation gas to lie further from the obscuring torus, while the fraction of high-excitation gas observed will follow a tighter dependence upon the angle at which the observer views the obscuring torus. We may therefore expect that intrinsically similar radio-loud AGN viewed at a variety of angles will have unequal [OIII] luminosities but roughly equal $H\alpha + [NII]$ luminosities (Baum & Heckman 1989b; Jackson & Browne 1990).

It will also be important to investigate whether [OIII]/ $H\alpha$ ratios of order unity are indicative of Seyfert-like nebular activity. We note that, in general, the majority of objects in our sample with $L_{[OIII]}/L_{H\alpha} \neq 1$ in (i.e. those galaxies significantly offset from the diagonal line in Fig. 9d) are BLRGs, with the exception of one FR I. Though we are unable to make statistically significant inferences with respect to these issues (as our sample consists of only 19 galaxies), further investigation into these line ratios and associated line ratio maps may yield important results.

4.2.3. Emission line luminosities vs. total radio power

In Figs. 11(a) and 11(b) we plot emission line luminosity vs. total radio power at 178 MHz for $H\alpha + [NII]$ and [OIII], respectively. We note a clear upward trend in both figures, consistent with the results of the comprehensive study by Willott et al. (1999), which also found a tight correlation be-

tween emission line and radio luminosity in flux limited samples of radio galaxies.

We discuss interpretations of this result in §4.3, but it is first important to frame the results of the above emission line luminosity comparisons in the context of ionized gas distribution morphologies.

4.2.4. Morphology of the extended narrow line regions

The low- and high- excitation narrow-line regions we observe in our sample, overall, exhibit extended and complex morphologies characterized by (e.g.) clumpy regions of emission (e.g. 3C 33), wispy tendrils (3C 136.1, 3C 319), extended filaments and lanes (3C 196.1, 3C 234), and bi-conical series of shells (3C 180). In general the morphologies observed in [OIII] mirror those in $H\alpha$ +[NII] with some important exceptions (e.g. 3C 136.1, 3C 196.1, 3C 227, 3C 285). We also note the presence of bright unresolved nuclear emission in the cores of every object with the exception of 3C 129 in [OIII] and 3C 285 in $H\alpha$ +[NII] and [OIII] (no clearly “point source-like” nucleus is apparent in our images for that object).

In Figs. 12(a) and 12(b) we compare the projected linear sizes of the line-emitting regions with both redshift and elliptical host galaxy effective radius (respectively). We have estimated the gas distribution sizes, in kpc, from the largest angular extent (L.A.S.) subtended by the high surface brightness emission (as projected on the sky). While this is a rough estimate, it provides important insights as evidenced by the weak upward trend of L.A.S. with redshift (Fig. 12a), implying that larger distributions of optical line emitting gas are found at higher redshifts.

Values for the effective radii R_{eff} in Fig. 12(b) are from Floyd et al. (2008) and Donzelli et al. (2007), and were derived from surface brightness profile fitting to *HST*/NICMOS *H*-band images (and some NIR imaging from TNG, in the case of Donzelli et al. 2007). While the methods employed by these two studies differ, their results are generally consistent, and any uncertainty introduced in plotting results from both papers is reflected in the characteristic error bars we have indicated in the figure. In light of these added uncertainties, however, we are unable to make any significant inferences, though L.A.S. and R_{eff} do appear weakly correlated for galaxies with $R_{\text{eff}} < 4$ kpc, while no such correlation is evident for those objects with $R_{\text{eff}} > 4$.

4.3. Physical interpretation of the trends observed

We have discussed three trends apparent in our data:

1. Emission line luminosity (both for $H\alpha$ + [NII] and [OIII]) appears positively correlated with the redshift of the host galaxy.
2. The $H\alpha$ + [NII] and [OIII] luminosities are also tightly correlated with total radio power at 178 MHz.
3. Projected sizes of the ionized gas distributions in our sample are positively correlated with host galaxy redshifts. That is, we observe larger line-emitting regions at greater distances.

The above results are consistent with those of (e.g.) Willott et al. (1999, 2003); Privon et al. (2008) (and references therein), as well as many other past studies of emission line gas in radio galaxies. The tight redshift-luminosity correlation in flux-limited samples results in the selection

TABLE 3
RADIO PROPERTIES

Source (1)	Type (2)	$S_{178 \text{ MHz}}$ (Jy) (3)	$\log P_{178 \text{ MHz}}$ ($\text{erg s}^{-1} \text{ Hz}^{-1}$) (4)
3C 33.0	FR II	49.0	33.65
3C 40.0	FR II	24.0	32.20
3C 78.0	FR I	15.0	32.71
3C 93.1	CSS	10.0	34.51
3C 129.0	FR I	21.0	32.67
3C 132.0	FR II	12.5	34.26
3C 136.1	FR II	13.0	33.39
3C 180.0	...	14.0	34.33
3C 196.1	CSS	14.5	34.32
3C 197.1	FR II	9.5	33.55
3C 219.0	FR II	44.0	34.54
3C 227.0	FR II	28.0	33.74
3C 234.0	FR II	29.0	34.47
3C 270.0	FR I	44.0	32.75
3C 285.0	FR II	10.5	33.23
3C 314.1	FR I	9.0	33.59
3C 319.0	FR II	17.0	34.20
3C 388.0	FR II	22.0	33.69
3C 390.3	FR II	44.0	33.55

REFERENCES. — Fanaroff & Riley 1974; Spinrad et al. 1985

NOTE. — (1) Source name; (2) Fanaroff-Riley classification; (3) 178 MHz flux density in Jy; (4) Log_{10} of radio power at 178 MHz, in erg s^{-1} .

of intrinsically brighter objects at higher redshifts. In radio flux density selected samples such as the 3CR, this is manifest in more powerful radio galaxies (FR IIs) inhabiting a higher redshift range than do their intrinsically lower-power counterparts (FR Is). Moreover, the alignment effect discussed in §1 suggests that propagation of the radio jet plays a role in the excitation of the ISM into line emission (Baum & Heckman 1989a; McCarthy 1993; Best et al. 2000). It is therefore unsurprising that more powerful radio galaxies appear associated with higher emission line luminosities, as they are able to collisionally excite and photoionize greater amounts of gas than are lower-power (and therefore lower-redshift) AGN (Baum & Heckman 1989a,b; Rawlings & Saunders 1991; Inskip et al. 2002a,b). As accretion disk radiative luminosity appears related to the jet kinetic energy flux (Baum & Heckman 1989b; Rawlings & Saunders 1991), this can be used to place constraints on the physics of the AGN. The greater mechanical energy input and number of ionizing photons provided by more powerful radio sources also explains the dependence of emission line region size on redshift: we expect the more powerful radio galaxies at higher redshifts to be capable of exciting gas at greater distances from the central engine, resulting in the observed trend.

It should also be noted that dense clouds of gas are observed on increasingly larger scales at higher redshifts, ultimately forming the vast Ly- α halos that surround the most powerful radio galaxies (van Ojik et al. 1997; Reuland et al. 2003). While this dependence of gas cloud density and extent on redshift is important for objects with $z > 0.6$ (the point near which the alignment effect precipitously tightens), it is not likely to contribute in any meaningful way to our comparatively low redshift sample at $z < 0.3$.

5. SUMMARY AND CONCLUDING REMARKS

In this paper we have presented *HST*/ACS narrow-band imaging of $H\alpha$ + [NII] and [OIII] λ 5007 line-emission in the central regions of 19 low-redshift radio galaxies from the 3CR

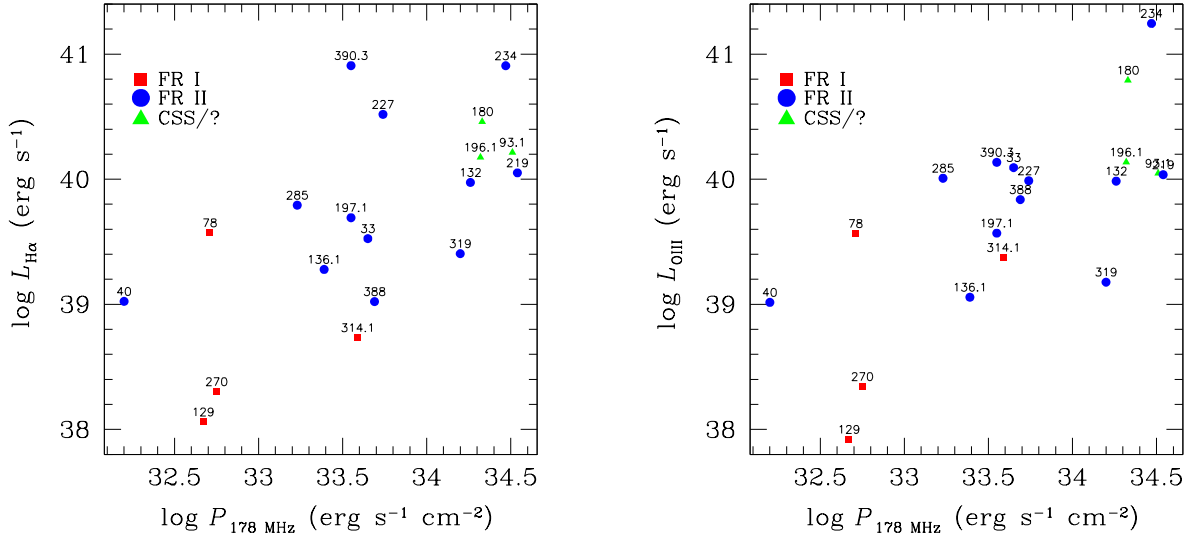


FIG. 11.— Emission line luminosity vs. total radio power at 178 MHz for (a) $H\alpha+[NII]$ and (b) $[OIII]$. Radio luminosities are from Spinrad et al. (1985). Red squares represent the four FR Is in our sample, while blue circles are FR IIs and green triangles represent those objects exhibiting a CSS or unclassified radio morphology. We note the clear upward trend in both figures, consistent with the results of the comprehensive study by Willott et al. (1999) which found a tight correlation between emission line and radio luminosity in flux limited samples of radio galaxies. See Table 3 for a summary of the radio properties in our sample.

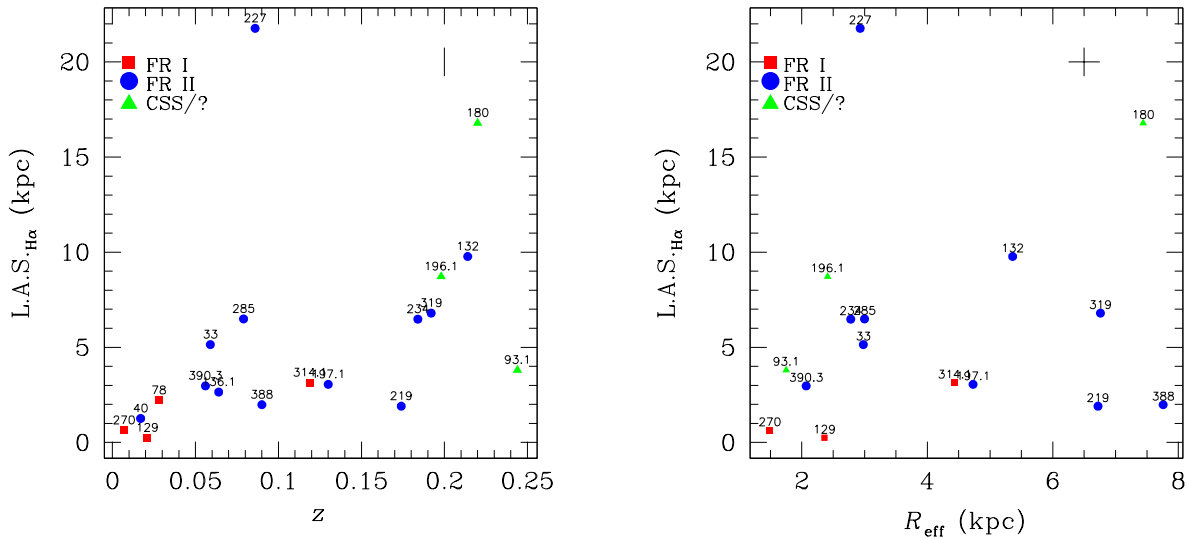


FIG. 12.— Comparison of the projected linear sizes of the extended high surface brightness $H\alpha+[NII]$ emission line regions with both (a) redshift and (b) effective radii R_{eff} of the host galaxies. The size estimates represent the largest angular size (L.A.S) of the narrow line regions detected in our $H\alpha+[NII]$ imaging. We do not plot the L.A.S. of the $[OIII]$ regions as their sizes generally mirror those of the $H\alpha+[NII]$ regions, with some important exceptions (see §4.2). Characteristic error bars appear in the upper right corner of each plot. The effective radii, in kpc, are from Floyd et al. (2008) and Donzelli et al. (2007) and were derived from surface brightness profile fitting to *HST*/NICMOS *H*-band images (and some NIR imaging from *Telescopio Nazionale Galileo* in the case of Donzelli et al. 2007). While the methods employed by these two studies differ, their results are generally consistent, and any uncertainty introduced in plotting results from both papers is reflected in the characteristic error bar we have indicated. We have omitted 3C 40, 3C 78, and 3C 136.1 from (b) as no estimate for their R_{eff} was available. Note the general upward trend of the L.A.S. with redshift, as well as a weaker upward trend with R_{eff} . The former result is consistent with the emission line study of Privon et al. (2008), and is expected given the tight redshift-luminosity correlation resulting in the selection of higher power sources at higher redshifts. The higher-power sources are likely able to ionize gas at greater distances from the central engine, contributing to the upward trend we observe.

catalog. We have chosen the 3CR as the basis for our sample as it is radio flux density selected at a frequency dominated by unbeamed radio lobes, and is therefore free from orientation bias with respect to all *HST* wavelengths. Moreover, the 3CR has been extensively covered by past ground- and space-based imaging and spectroscopy programs, yielding a robust, cross-spectrum database containing galaxies exhibiting a wide variety of intrinsic characteristics. We limit our sample to the low-redshift subset ($z < 0.3$) of the 3CR to maximize spatial resolution, as well as to ensure that the emission lines fall

within the redshift range of high sensitivity. The ACS observations were carried out during *HST* Cycle 15, and in total, 19 galaxies were observed prior to failure of the instrument in January 2007. Reduction of these data was performed independently of the automated OTFR pipeline so as to improve on flat-fielding and to more proactively clean the images of cosmic rays and hot pixels. In addition, contribution from continuum was subtracted to yield effectively pure emission line images.

We have compared the resulting emission line luminosities

with both redshift and total radio power, finding weak positive correlations for each. We have also noted an upward trend between the projected size of the emission line gas distributions and redshift. These results are consistent with those from past studies, and we have interpreted the apparent trends to be a result of higher power radio galaxies, preferentially found at greater distances, which can shock and photoionize greater amounts of the ISM further away from the nucleus, thus resulting in brighter and more extended emission-line regions.

Regardless of the interpretation, recombination times for warm gas ($T \sim 10^4$ K) are of order 10^3 years (Osterbrock & Ferland 2006), while lifetimes of radio sources are of order 10^8 years. The process by which the gas is ionized should therefore be ongoing throughout the lifetime of the source, implying a strong connection between AGN activity and observed emission line properties. The sensitive, high spatial resolution images presented in this paper may therefore enrich future works studying jets propagating through the ISM, and their relationship with extended and compact

star formation regions as well as X-ray coronal halos. Future emission line studies of larger samples of radio galaxies may also deepen understanding of radio-loud unification schemes, as warm optical line emitting gas traces fundamental energy transport processes coupled to feedback at the interface of the AGN and its surrounding medium.

We are indebted to the anonymous referee whose comments led to the improvement of this work. We thank George Privon for helpful discussions and access to data. G. R. T. acknowledges A. N. S. and support from NASA grant HST-GO-10882.01-A, as well as the New York Space Grant Consortium. This research made use of the NASA Astrophysics Data System bibliographic services and the NASA/IPAC Extragalactic Database, operated by the Jet Propulsion Laboratory, California Institute of Technology, under contract with NASA.

REFERENCES

- Allen, M. G., Sparks, W. B., Koekemoer, A., Martel, A. R., O'Dea, C. P., Baum, S. A., Chiaberge, M., Macchetto, F. D., & Miley, G. K. 2002, *ApJS*, 139, 411
- Baum, S. A., & Heckman, T. 1989a, *ApJ*, 336, 681
- , 1989b, *ApJ*, 336, 702
- Baum, S. A., Heckman, T., & van Breugel, W. 1990, *ApJS*, 74, 389
- Baum, S. A., Heckman, T. M., Bridle, A., van Breugel, W. J. M., & Miley, G. K. 1988, *ApJS*, 68, 643
- Bell, E. F., Wolf, C., Meisenheimer, K., Rix, H.-W., Borch, A., Dye, S., Kleinheinrich, M., Wisotzki, L., & McIntosh, D. H. 2004, *ApJ*, 608, 752
- Bennett, A. S. 1962a, *MNRAS*, 125, 75
- , 1962b, *MmRAS*, 68, 163
- Best, P. N., Röttgering, H. J. A., & Longair, M. S. 2000, *MNRAS*, 311, 23
- Blanton, E. L., Sarazin, C. L., McNamara, B. R., & Wise, M. W. 2001, *ApJ*, 558, L15
- Buttiglione, S., Capetti, A., Celotti, A., Axon, D. J., Chiaberge, M., Macchetto, F. D., & Sparks, W. B. 2009, *A&A*, 495, 1033
- Capetti, A., Axon, D. J., Macchetto, F. D., Marconi, A., & Winge, C. 1999, *ApJ*, 516, 187
- Carleton, N. P., Willmer, S. P., Rudy, R. J., & Tokunaga, A. T. 1984, *ApJ*, 284, 523
- Chambers, K. C., Miley, G. K., & van Breugel, W. 1987, *Nature*, 329, 604
- Chiaberge, M. 2004, in *Multiwavelength AGN Surveys*, ed. R. Mújica & R. Maiolino, 217–+
- Chiaberge, M., Capetti, A., & Celotti, A. 2000, *A&A*, 355, 873
- Chiaberge, M., Macchetto, F. D., Sparks, W. B., Capetti, A., Allen, M. G., & Martel, A. R. 2002, *ApJ*, 571, 247
- Cowie, L. L., Songaila, A., Hu, E. M., & Cohen, J. G. 1996, *AJ*, 112, 839
- de Koff, S., Best, P., Baum, S. A., Sparks, W., Röttgering, H., Miley, G., Golombek, D., Macchetto, F., & Martel, A. 2000, *ApJS*, 129, 33
- di Matteo, T., Springel, V., & Hernquist, L. 2005, *Nature*, 433, 604
- Donzelli, C. J., Chiaberge, M., Macchetto, F. D., Madrid, J. P., Capetti, A., & Marchesini, D. 2007, *ApJ*, 667, 780
- Faber, S. M., Willmer, C. N. A., Wolf, C., Koo, D. C., Weiner, B. J., Newman, J. A., Im, M., Coil, A. L., Conroy, C., Cooper, M. C., Davis, M., Finkbeiner, D. P., Gerke, B. F., Gebhardt, K., Groth, E. J., Guhathakurta, P., Harker, J., Kaiser, N., Kassin, S., Kleinheinrich, M., Konidaris, N. P., Kron, R. G., Lin, L., Luppino, G., Madgwick, D. S., Meisenheimer, K., Noeske, K. G., Phillips, A. C., Sarajedini, V. L., Schiavon, R. P., Simard, L., Szalay, A. S., Vogt, N. P., & Yan, R. 2007, *ApJ*, 665, 265
- Fabian, A. C. 1999, *MNRAS*, 308, L39
- Fanaroff, B. L., & Riley, J. M. 1974, *MNRAS*, 167, 31P
- Ferrarese, L., & Merritt, D. 2000, *ApJ*, 539, L9
- Floyd, D. J. E., Axon, D., Baum, S., Capetti, A., Chiaberge, M., Macchetto, D., Madrid, J., Miley, G., O'Dea, C. P., Perlman, E., Quillen, A., Sparks, W., & Tremblay, G. 2008, *ApJS*, 177, 148
- Floyd, D. J. E., Laing, R., Chiaberge, M., Perlman, E., Sparks, W., Macchetto, D., Madrid, J., Axon, D., O'Dea, C. P., Baum, S., Quillen, A., Miley, G., & Capetti, A. 2006, *ApJ*, 643, 660
- Fosbury, R. A. E. 1986, in *Astrophysics and Space Science Library*, Vol. 121, *Structure and Evolution of Active Galactic Nuclei*, ed. G. Giuricin, M. Mezzetti, M. Ramella, & F. Mardirosian, 297–306
- Gebhardt, K., Kormendy, J., Ho, L. C., Bender, R., Bower, G., Dressler, A., Faber, S. M., Filippenko, A. V., Green, R., Grillmair, C., Lauer, T. R., Magorrian, J., Pinkney, J., Richstone, D., & Tremaine, S. 2000, *ApJ*, 543, L5
- Hansen, L., Jorgensen, H. E., & Norgaard-Nielsen, H. U. 1987, *A&AS*, 71, 465
- Heckman, T. M., Illingworth, G. D., Miley, G. K., & van Breugel, W. J. M. 1985, *ApJ*, 299, 41
- Hopkins, P. F., Hernquist, L., Cox, T. J., Di Matteo, T., Robertson, B., & Springel, V. 2005, *ApJ*, 630, 716
- Inskip, K. J., Best, P. N., Rawlings, S., Longair, M. S., Cotter, G., Röttgering, H. J. A., & Eales, S. 2002a, *MNRAS*, 337, 1381
- Inskip, K. J., Best, P. N., Röttgering, H. J. A., Rawlings, S., Cotter, G., & Longair, M. S. 2002b, *MNRAS*, 337, 1407
- Jackson, N., & Browne, I. W. A. 1990, *Nature*, 343, 43
- Jackson, N., & Rawlings, S. 1997, *MNRAS*, 286, 241
- Jaffe, W., Ford, H. C., Ferrarese, L., van den Bosch, F., & O'Connell, R. W. 1993, *Nature*, 364, 213
- Koekemoer, A. M., Fruchter, A. S., Hook, R. N., & Hack, W. 2002, in *The 2002 HST Calibration Workshop : Hubble after the Installation of the ACS and the NICMOS Cooling System*, ed. S. Arribas, A. Koekemoer, & B. Whitmore, 337–+
- Madrid, J. P., Chiaberge, M., Floyd, D., Sparks, W. B., Macchetto, D., Miley, G. K., Axon, D., Capetti, A., O'Dea, C. P., Baum, S., Perlman, E., & Quillen, A. 2006, *ApJS*, 164, 307
- Magorrian, J., Tremaine, S., Richstone, D., Bender, R., Bower, G., Dressler, A., Faber, S. M., Gebhardt, K., Green, R., Grillmair, C., Kormendy, J., & Lauer, T. 1998, *AJ*, 115, 2285
- Martel, A. R., Baum, S. A., Sparks, W. B., Wyckoff, E., Biretta, J. A., Golombek, D., Macchetto, F. D., de Koff, S., McCarthy, P. J., & Miley, G. K. 1999, *ApJS*, 122, 81
- McCarthy, P. J. 1988, PhD thesis, AA(California Univ., Berkeley)
- , 1993, *ARA&A*, 31, 639
- McCarthy, P. J., Spinrad, H., & van Breugel, W. 1995, *ApJS*, 99, 27
- McNamara, B. R., Wise, M., Nulsen, P. E. J., David, L. P., Sarazin, C. L., Bautz, M., Markevitch, M., Vikhlinin, A., Forman, W. R., Jones, C., & Harris, D. E. 2000, *ApJ*, 534, L135
- Osterbrock, D. E., & Ferland, G. J. 2006, *Astrophysics of gaseous nebulae and active galactic nuclei (Astrophysics of gaseous nebulae and active galactic nuclei, 2nd. ed. by D.E. Osterbrock and G.J. Ferland. Sausalito, CA: University Science Books, 2006)*
- Padovani, P., & Urry, C. M. 1992, *ApJ*, 387, 449
- Perlman, E. S., Padgett, C. A., Georganopoulos, M., Sparks, W. B., Biretta, J. A., O'Dea, C. P., Baum, S. A., Birkinshaw, M., Worrall, D. M., Dulwich, F., Jester, S., Martel, A., Capetti, A., & Leahy, J. P. 2006, *ApJ*, 651, 735
- Prieto, M. A. 1993, *Ap&SS*, 205, 185
- Privon, G. C., O'Dea, C. P., Baum, S. A., Axon, D. J., Kharb, P., Buchanan, C. L., Sparks, W., & Chiaberge, M. 2008, *ApJS*, 175, 423
- Quillen, A. C., & Bower, G. A. 1999, *ApJ*, 522, 718
- Rawlings, S., & Saunders, R. 1991, *Nature*, 349, 138

- Reuland, M., van Breugel, W., Röttgering, H., de Vries, W., Stanford, S. A., Dey, A., Lacy, M., Bland-Hawthorn, J., Dopita, M., & Miley, G. 2003, *ApJ*, 592, 755
- Reynolds, C. S., Heinz, S., & Begelman, M. C. 2002, *MNRAS*, 332, 271
- Ruszkowski, M., & Begelman, M. C. 2002, *ApJ*, 581, 223
- Schmitt, H. R., Pringle, J. E., Clarke, C. J., & Kinney, A. L. 2002, *ApJ*, 575, 150
- Silk, J., & Rees, M. J. 1998, *A&A*, 331, L1
- Silverman, J. D., Mainieri, V., Lehmer, B. D., Alexander, D. M., Bauer, F. E., Bergeron, J., Brandt, W. N., Gilli, R., Hasinger, G., Schneider, D. P., Tozzi, P., Vignali, C., Koekemoer, A. M., Miyaji, T., Popesso, P., Rosati, P., & Szokoly, G. 2008, *ApJ*, 675, 1025
- Simkin, S. M. 1979, *ApJ*, 234, 56
- Sparks, W. B., Baum, S. A., Biretta, J., Macchetto, F. D., & Martel, A. R. 2000, *ApJ*, 542, 667
- Sparks, W. B., Golombek, D., Baum, S. A., Biretta, J., de Koff, S., Macchetto, F., McCarthy, P., & Miley, G. K. 1995, *ApJ*, 450, L55+
- Spinrad, H., Marr, J., Aguilar, L., & Djorgovski, S. 1985, *PASP*, 97, 932
- Tremblay, G. R., Chiaberge, M., Donzelli, C. J., Quillen, A. C., Capetti, A., Sparks, W. B., & Macchetto, F. D. 2007, *ApJ*, 666, 109
- Tremblay, G. R., Quillen, A. C., Floyd, D. J. E., Noel-Storr, J., Baum, S. A., Axon, D., O'Dea, C. P., Chiaberge, M., Macchetto, F. D., Sparks, W. B., Miley, G. K., Capetti, A., Madrid, J. P., & Perlman, E. 2006, *ApJ*, 643, 101
- van Ojik, R., Roettgering, H. J. A., Miley, G. K., & Hunstead, R. W. 1997, *A&A*, 317, 358
- Verdoes Kleijn, G. A., & de Zeeuw, P. T. 2005, *A&A*, 435, 43
- Willott, C. J., Rawlings, S., Blundell, K. M., & Lacy, M. 1999, *MNRAS*, 309, 1017
- Willott, C. J., Simpson, C., Almaini, O., Manners, J. C., Johnson, O., Lawrence, A., Dunlop, J. S., Ivison, R. J., Rawlings, S., González-Solares, E., Pérez-Fournon, I., Serjeant, S., Oliver, S. J., Roche, N. D., Mann, R. G., & Rowan-Robinson, M. 2003, *MNRAS*, 339, 397